Author Manuscript

Author Manuscript

Author Manuscript

Author Manuscript

HHS Public Access

Author manuscript

Cell Rep. Author manuscript; available in PMC 2022 October 05.

Published in final edited form as:

Cell Rep. 2022 September 20; 40(12): 111393. doi:10.1016/j.celrep.2022.111393.

SMN controls neuromuscular junction integrity through U7 snRNP

Sarah Tisdale[1,2,3], **Meaghan Van Alstyne**[1,2,3], **Christian M. Simon**[1,2,4], **George Z. Mentis**[1,2,3], **Livio Pellizzoni**[1,2,3,5,*]

[1]Center for Motor Neuron Biology and Disease, Columbia University, New York, NY 10032, USA

[2]Department of Pathology and Cell Biology, Columbia University, New York, NY 10032, USA

[3]Department of Neurology, Columbia University, New York, NY 10032, USA

[4]Present address: Carl-Ludwig-Institute for Physiology, Leipzig University, Leipzig 04103, Germany

[5]Lead contact

SUMMARY

The neuromuscular junction (NMJ) is an essential synapse whose loss is a key hallmark of the neurodegenerative disease spinal muscular atrophy (SMA). Here, we show that activity of the SMA-determining SMN protein in the assembly of U7 small nuclear ribonucleoprotein (snRNP)—which functions in the 3′-end processing of replication-dependent histone mRNAs—is required for NMJ integrity. Co-expression of U7-specific Lsm10 and Lsm11 proteins selectively enhances U7 snRNP assembly, corrects histone mRNA processing defects, and rescues key structural and functional abnormalities of neuromuscular pathology in SMA mice—including NMJ denervation, decreased synaptic transmission, and skeletal muscle atrophy. Furthermore, U7 snRNP dysfunction drives selective loss of the synaptic organizing protein Agrin at NMJs innervating vulnerable muscles of SMA mice. These findings reveal a direct contribution of U7 snRNP dysfunction to neuromuscular pathology in SMA and suggest a role for histone gene regulation in maintaining functional synaptic connections between motor neurons and muscles.

In brief

NMJ denervation is a hallmark of SMA. Through selective restoration of U7 snRNP biogenesis in SMA mice, Tisdale et al. reveal a role for SMN-mediated U7 snRNP assembly and histone mRNA processing in controlling NMJ integrity through Agrin expression, uncovering RNA-mediated disease mechanisms and linking U7 function to neuromuscular development.

This is an open access article under the CC BY-NC-ND license (http://creativecommons.org/licenses/by-nc-nd/4.0/).

*Correspondence: lp2284@cumc.columbia.edu.

AUTHOR CONTRIBUTIONS

S.T. and L.P. conceived the study. S.T., M.V.A., and C.M.S. performed experiments. S.T., M.V.A., C.M.S., G.Z.M., and L.P. participated in experimental design and data analysis. S.T. and L.P. wrote the manuscript with contributions from all authors.

DECLARATION OF INTERESTS

The authors declare no competing interests.

SUPPLEMENTAL INFORMATION

Supplemental information can be found online at https://doi.org/10.1016/j.celrep.2022.111393.

Author Manuscript Author Manuscript Author Manuscript Author Manuscript

Graphical Abstract

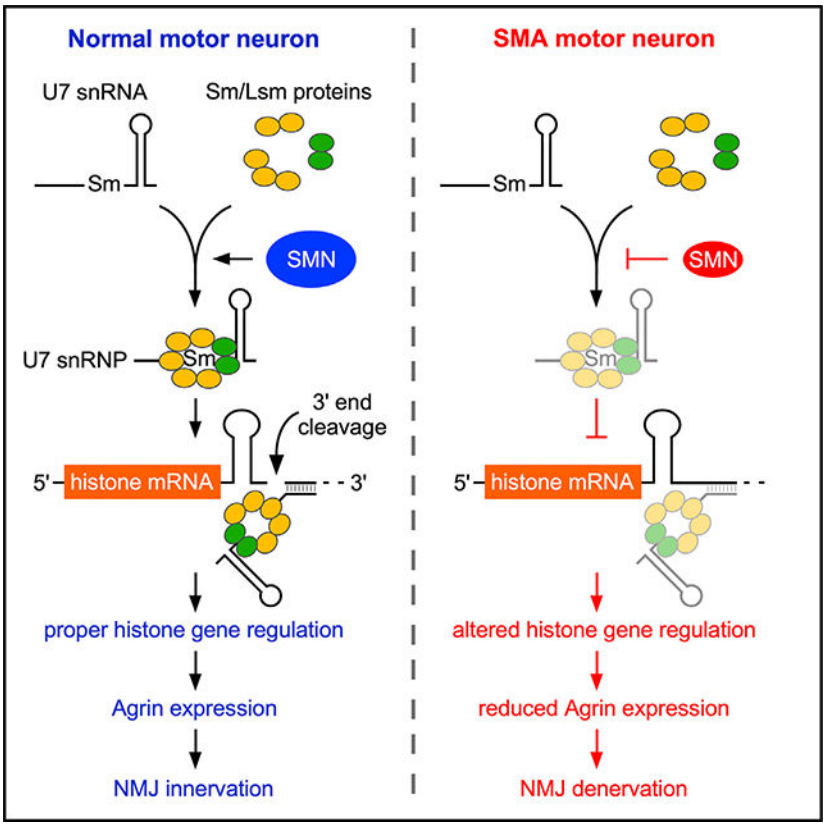

INTRODUCTION

The neuromuscular junction (NMJ) is a specialized chemical synapse that controls motor behaviors indispensable for human life such as breathing, swallowing, and movement. NMJ innervation and function are strongly affected in some of the most severe and often-fatal neuromuscular diseases such as spinal muscular atrophy (SMA) (Mercuri et al., 2020; Tisdale and Pellizzoni, 2015), amyotrophic lateral sclerosis (ALS) (Gromova and La Spada, 2020), and myasthenia gravis (Gilhus et al., 2019), as well as by exposure to lethal toxins and venoms (Meunier et al., 2002). Importantly, RNA dysregulation is emerging as a driver of neuromuscular pathology in ALS and SMA, among other neurodegenerative diseases (Nussbacher et al., 2019; Tisdale and Pellizzoni, 2015). However, the RNA-mediated mechanisms controlling the biology of this specialized synapse that go awry in disease are poorly understood. Understanding this connection has the potential to uncover unknown aspects of NMJ biology in health and disease that have fundamental biomedical relevance.

NMJ denervation of vulnerable axial and proximal muscles is a hallmark of SMA (Mercuri et al., 2020; Tisdale and Pellizzoni, 2015), which is caused by a ubiquitous deficiency in the survival motor neuron (SMN) protein owing to homozygous deletion or mutation of the *SMN1* gene (Lefebvre et al., 1995; Wirth et al., 2020). SMN is part of a multi-functional protein complex with essential roles in RNA regulation (Donlin-Asp et al., 2016; Li et

Author Manuscript Author Manuscript Author Manuscript Author Manuscript

al., 2014), including the assembly of small nuclear ribonucleoproteins (snRNPs) of the spliceosomes that catalyze splicing of U2- and U12-type introns (Meister et al., 2001; Pellizzoni et al., 2002), as well as the U7 snRNP that is required for the processing of histone mRNAs (Pillai et al., 2003; Tisdale et al., 2013). Determining the relative contribution of specific SMN-dependent RNA pathways to neuromuscular pathology in SMA is critical for understanding disease mechanisms and may also help to identify therapeutic strategies that could complement SMN-inducing treatments. To reach this goal, a powerful approach is to selectively correct the most proximal functional defects of SMN deficiency in each RNA pathway without altering SMN expression and to assess the resulting effects on disease pathology in animal models. In this context, the injection of purified snRNPs in SMN-deficient embryos was shown to suppress motor axon outgrowth deficits in a zebrafish model of SMA (Winkler et al., 2005), while selective enhancement of U12 splicing by adenoassociated virus serotype 9 (AAV9)-mediated overexpression of minor snRNAs prevented the loss of proprioceptive synapses onto motor neurons in SMA mice (Osman et al., 2020). These and other studies highlighted the contribution of splicing dysregulation induced by SMN deficiency to sensory-motor dysfunction and the death of motor neurons in SMA models (Van Alstyne et al., 2018; Lotti et al., 2012; Osman et al., 2020; Simon et al., 2017, 2019; Winkler et al., 2005). However, which of the numerous functions of SMN account for NMJ denervation and muscle fiber atrophy in SMA remains to be established.

Histones are highly conserved nuclear proteins that facilitate chromatin compaction and are central to gene regulation. Metazoan replication-dependent histones are encoded by a class of genes whose mRNAs lack introns and poly(A) tails (Marzluff et al., 2008). The only processing event to occur on histone precursor mRNA is a single 3′-end endonucleolytic cleavage that is both dependent on U7 snRNP function and required for proper regulation of histone gene expression (Dominski and Marzluff, 2007; Marzluff et al., 2008). We previously demonstrated that SMN deficiency disrupts U7 snRNP biogenesis and histone mRNA 3′-end processing in SMA mice and human patients (Tisdale et al., 2013), but a direct pathogenic role for the perturbation of this RNA pathway in the disease process has not been established. Moreover, while it is widely recognized that histone mRNA 3′-end processing is key for dividing cells to ensure that proper amounts of histones are synthesized to match the requirement for genome replication during S phase (Dominski and Marzluff, 2007; Marzluff et al., 2008), this need is not shared by neurons because they are postmitotic and it is unknown whether U7 function is important for the biology of neurons.

Designed to address these outstanding questions through the selective restoration of U7 snRNP biogenesis and function in a mouse model of SMA, this study identifies the specific SMN-dependent RNA pathway driving NMJ denervation in SMA and reveals an unexpected role for U7-mediated histone mRNA processing in motor neuron biology and disease.

RESULTS

Lsm10 and Lsm11 co-expression enhances U7 snRNP assembly

SMN mediates the assembly of Sm proteins onto their respective snRNA substrates to generate functional snRNPs that carry out pre-mRNA splicing (Meister et al., 2001;

Author Manuscript Author Manuscript Author Manuscript Author Manuscript

Pellizzoni et al., 2002). In addition, specialized SMN complexes in which the Sm-like proteins Lsm10 and Lsm11 replace SmD1 and SmD2 of spliceosomal snRNPs mediate the assembly of U7 snRNP (Pillai et al., 2001, 2003; Tisdale et al., 2013) (Figure 1A), which functions not in splicing but in histone mRNA processing (Dominski and Marzluff, 2007; Marzluff et al., 2008). These SMN complexes are limiting owing to the low abundance of Lsm10 and Lsm11 proteins relative to the amounts of Sm proteins that are assembled on spliceosomal snRNPs (Pillai et al., 2001, 2003). We, therefore, reasoned that increasing the levels of U7-specific Lsm10 and Lsm11 could be a means to selectively enhance U7 snRNP assembly. To test this, we generated NIH3T3-Smn_{RNAi} cell lines with doxycycline (Dox)-regulated RNA interference (RNAi) knockdown of endogenous SMN (Lotti et al., 2012; Ruggiu et al., 2012; Tisdale et al., 2013) that overexpressed FLAG-tagged Lsm10 and Lsm11 either alone or in combination (Figures S1A and S1B). Immunoprecipitation experiments demonstrated that epitope-tagged Lsm10 and Lsm11 specifically incorporate into endogenous U7 snRNPs in these cell lines (Figure S1C). Using *in vitro* snRNP assembly assays with radioactive snRNAs (Pellizzoni et al., 2002; Tisdale et al., 2013), we found that the co-expression of Lsm10 and Lsm11—but neither on its own—specifically and strongly increased U7 but not U1 snRNP assembly without changes in SMN levels (Figures 1B and 1C). To determine the effects of Lsm10/11 overexpression *in vivo*, we first developed a single-cassette vector for the co-expression of FLAG-tagged Lsm10 and Lsm11 that also robustly enhanced U7 snRNP assembly *in vitro* (Figures S1D–S1F). We then delivered an AAV9 vector harboring this cassette under a CAG promoter in the central nervous system (CNS) of wild-type (WT) mice at P0 by intracerebroventricular injection followed by an analysis of snRNP assembly at P11 (Figure S2A). AAV9-Lsm10/11 specifically increased U7 but not U1 snRNP assembly in brain extracts (Figures S2B and S2C). Thus, the co-expression of Lsm10 and Lsm11 is necessary and sufficient to selectively increase SMN-dependent U7 snRNP assembly both *in vitro* and *in vivo*.

We next investigated the effects of Lsm10/11 co-expression when U7 biogenesis is strongly decreased by SMN deficiency (Tisdale et al., 2013). Although both Smn_{RNAi} and Lsm10/11-Smn_{RNAi} cells display a similar Dox-dependent, RNAi-mediated knockdown of Smn to approximately 10% of normal levels, Lsm10/11 co-expression led to a strong increase in the assembly of U7 but not U1 snRNP in SMN-deficient cells (Figures 1D and 1E). Furthermore, Lsm10/11 co-expression specifically corrected the decrease in the endogenous levels of U7 but not U12 snRNA induced by SMN deficiency in NIH3T3 (Figures 1F and 1G) (Lotti et al., 2012; Tisdale et al., 2013). Therefore, Lsm10/11 co-expression can selectively increase both U7 snRNP assembly and steady-state U7 levels in SMN-deficient mammalian cells.

To determine the impact of Lsm10/11 co-expression on defective U7 biogenesis in a mouse model of SMA, we used AAV9-mediated gene delivery of Lsm10/11 in SMNΔ7 mice (Le et al., 2005). While the overexpression of Lsm10 and Lsm11 did not alter the levels of SMN relative to green fluorescent protein (GFP)-treated SMA mice (Figures S2D and S2E), AAV9-Lsm10/11 partially corrected the severe decrease in U7 snRNP assembly induced by SMN deficiency (Figures S2F and S2G). Moreover, AAV9-Lsm10/11 significantly increased endogenous U7 snRNA levels in the liver of SMA mice (Figures S2H and S2I). Such an increase was not detected in spinal cord, likely owing to the different efficiency of tissue

Author Manuscript Author Manuscript Author Manuscript Author Manuscript

transduction by AAV9, which is widespread in the liver but more limited in the CNS, as indicated by the spatial profile of viral-mediated GFP expression (Figures S2J and S2K), consistent with previous studies (Van Alstyne et al., 2021). Accordingly, Flag-tagged Lsm10 and Lsm11 proteins could be detected in the liver but not the spinal cord of AAV9 injected SMA mice by whole tissue western blot analysis (Figure S2E). Together, these results indicate that Lsm10/11 co-expression selectively enhances U7 snRNP biogenesis in SMA mice in the absence of SMN modulation.

Selective correction of histone gene dysregulation by Lsm10/11 in SMA models

The only known cellular function of U7 snRNP is its activity in the 3′-end processing of replication-dependent histone mRNAs (Dominski and Marzluff, 2007; Marzluff et al., 2008), which is disrupted in SMA as a direct consequence of the decreased levels of U7 snRNP assembly induced by SMN deficiency (Tisdale et al., 2013). Remarkably, Lsm10/11 co-expression robustly corrected the accumulation of uncleaved, 3′-extended histone mRNAs in SMN-deficient NIH3T3cells (Figure 2A) and in tissue of SMA mice (Figures 2C and S3E). Similar results were found by measuring the normalized ratio of individual 3′-extended mRNA isoforms relative to the corresponding total levels (precursor and mature) of each histone mRNA (Figure S3A), which confirmed direct modulation of the efficiency of 3′-end processing. Importantly, the effects were also highly specific because several SMN-dependent RNA processing defects unrelated to U7 function (Van Alstyne et al., 2018; Lotti et al., 2012; Tisdale et al., 2013) were not improved (Figures S3B–S3D and S3F–S3H). Thus, Lsm10/11 co-expression results in the selective correction of U7-mediated histone mRNA 3′-end processing deficits induced by SMN deficiency both *in vitro* and *in vivo*.

Lsm10/11 co-expression restored histone protein levels that are decreased in SMN-deficient NIH3T3cells without an impact on cell proliferation (Figures 2B, S4A, and S4B) (Tisdale et al., 2013), indicating that they result directly from U7-dependent dysregulation of histone mRNA 3′-end processing and not indirectly from halted cell division. In contrast, we found that histone levels were not globally affected in the spinal cord of SMA mice at P11 (Figure S4C). This could reflect the fact that the threshold of U7 snRNP reduction necessary to impair histone synthesis is only reached in the subset of spinal cells that are more vulnerable to the disease, which is consistent with disruption of snRNP biogenesis being more prominent in SMA motor neurons than other spinal cells (Van Alstyne et al., 2018; Ruggiu et al., 2012; Simon et al., 2017; Tisdale and Pellizzoni, 2015). Therefore, we sought to investigate histone expression in disease-relevant motor neurons by immunostaining. Since each of the core histones represents a family of proteins encoded by multiple genes that cannot be distinguished using available antibodies (Marzluff et al., 2008), we performed immunostaining against H2AX—a single copy histone gene that undergoes U7-dependent 3′-end processing and is affected by SMN deficiency (Tisdale et al., 2013). We found a decrease in H2AX expression in motor neurons from SMA mice injected with AAV9-GFP relative to WT motor neurons that was corrected by AAV9-Lsm10/11 injection (Figures 2D and 2E). Although we were unable to directly document the overexpression of Lsm10/11 proteins in SMA motor neurons owing to the lack of suitable antibodies for immunohistochemistry, the large number of motor neurons analyzed together with the

Author Manuscript Author Manuscript Author Manuscript Author Manuscript

high efficiency (approximately 70%) of their transduction by AAV9 (Figures S2J and S2K) ensures the reliability of the differences in H2AX levels measured across experimental groups and the significant increase associated with Lsm10/11 co-expression. Thus, SMN deficiency can affect histone expression in SMA motor neurons and correction by Lsm10/11 indicates that this defect is downstream of U7 snRNP dysfunction.

U7 snRNP dysfunction contributes to neuromuscular pathology in SMA mice

Having established Lsm10/11 co-expression as a means for the selective improvement of defective U7 biogenesis and histone mRNA 3′-end processing, which represent the most proximal molecular events linked to the dysfunction of SMN in this RNA pathway, we next sought to assess their contribution to the disease process. To do so, we investigated the effects of AAV9-Lsm10/11 injection on the phenotype of SMA mice using AAV9-GFP and AAV9-SMN as negative and positive controls, respectively. AAV9-Lsm10/11 moderately improved motor function in SMA mice without affecting either weight or survival compared with GFP-injected SMA mice (Figures S5A–S5C), while AAV9-SMN robustly corrected all parameters, as expected (Van Alstyne et al., 2021; Foust et al., 2010; Passini et al., 2010; Simon et al., 2019).

To determine which elements of the severe neuromuscular phenotype of SMA mice could be improved by Lsm10/11, we first analyzed synaptic transmission at the NMJ by performing EMG recordings from the quadratus lumborum (QL), a disease-relevant, axial muscle, upon evoked stimulation of the L1 ventral root using the *ex vivo* spinal cord preparation. Remarkably, the amplitude of the compound muscle action potential that is ablated in GFP-injected SMA mice relative to WT controls at P11 was strongly improved by AAV9-Lsm10/11, although not to the same extent as SMN restoration (Figures 3A and 3B). The effects were specific to NMJ transmission, because the decrease in the amplitude of the compound motor neuron output upon stimulation of proprioceptive afferent fibers in the L1 dorsal root was not improved by AAV9-Lsm10/11 in SMA mice (Figures 4A and 4B). Importantly, while approximately 40% of NMJs were fully denervated in the QL of SMA mice treated with AAV-GFP, this defect was robustly corrected by AAV9-Lsm10/11 (Figures 3C and 3D). In contrast, the loss of VGlut1^{+} proprioceptive sensory synapses onto the somata of L1 motor neurons of GFP-treated SMA mice at P11 was rescued by AAV9-SMN but not AAV9-Lsm10/11 (Figures 4C and 4D). Lsm10/11 co-expression in SMA mice had also no effect on the loss of vulnerable L1 motor neurons (Figures 4E and 4F) and L5 medial motor column motor neurons (Figures 4G and 4H). Altogether, these results demonstrate that enhancement of U7 snRNP biogenesis through Lsm10/11 co-expression strongly improves NMJ innervation and function in SMA mice, while the lack of correction of deafferentation and death of SMA motor neurons supports the selectivity of the effects because these pathogenic events have been previously linked to SMN-dependent splicing changes unrelated to U7 function (Van Alstyne et al., 2018; Osman et al., 2020; Simon et al., 2017, 2019).

Dysfunction and loss of NMJs contribute to skeletal muscle atrophy, a hallmark of SMA pathology (Mercuri et al., 2020; Tisdale and Pellizzoni, 2015; Wirth et al., 2020), and the myofiber size in the triceps brachii is strongly decreased in AAV9-GFP-treated SMA

Author Manuscript Author Manuscript Author Manuscript Author Manuscript

mice relative to WT mice at P11 (Figures 3E and 3F). Remarkably, treatment with AAV9-Lsm10/11, similar to AAV9-SMN, significantly improved this phenotype in SMA mice (Figures 3E and 3F) as further highlighted by an increased proportion of large-sized myofibers (Figure S5D), revealing that U7 snRNP restoration improves skeletal muscle atrophy in SMA mice.

SMN regulates Agrin expression at the NMJ through U7 snRNP

The identification of impaired U7 snRNP assembly as the upstream trigger of a cascade leading to motor neuron denervation and muscle atrophy in SMA mice raised the question as to which downstream effector(s) could directly mediate the distal effects of U7 dysfunction at the NMJ. A candidate emerging from recent studies (Boido et al., 2018; Feng et al., 2021; Kaifer et al., 2020; Kim et al., 2017) was Agrin—an essential NMJ organizer that promotes clustering of post-synaptic acetylcholine receptors (AChR) during development (Gautam et al., 1996; Nitkin et al., 1987) and is also required for postnatal NMJ maintenance (Samuel et al., 2012). Since increasing Agrin levels or its associated signaling cascade has been shown to ameliorate NMJ pathology of SMA mice in a manner similar to Lsm10/11 co-expression (Boido et al., 2018; Feng et al., 2021; Kaifer et al., 2020; Kim et al., 2017), we sought to investigate possible links between Agrin and SMN-regulated U7 snRNP assembly. Motor neuron-derived Agrin isoforms (Z^+ Agrin) have greatly increased potency in AChR clustering owing to an amino acid insertion resulting from the inclusion of Z exons (Figure 5A) (Burgess et al., 1999; Ferns et al., 1992). We found that the levels of total (with or without Z exons) and Z exon-skipped (ΔZ) Agrin mRNAs were similar in the spinal cord of WT and SMA mice at P6 (Figure 5A). We then analyzed lumbar motor neurons innervating the QL and iliopsoas muscles, which were isolated from WT and SMA mice by laser capture microdissection as previously described (Van Alstyne et al., 2018; Lotti et al., 2012). Interestingly, vulnerable SMA motor neurons had lower levels of ΔZ Agrin mRNAs (Figure 5B), and total Agrin mRNAs were also decreased, but this difference did not reach statistical significance (Figure 5B). The increased levels of 3′-extended H1c transcripts confirmed U7 snRNP dysfunction in SMA motor neurons (Figure 5B) (Tisdale et al., 2013); the induction of Cdkn1a mRNA was used as a control for U7-independent RNA dysregulation (Figure 5B) (Ruggiu et al., 2012; Simon et al., 2017; Tisdale et al., 2013). These results suggest that transcript-level changes, rather than previously reported splicing dysregulation (Zhang et al., 2013), may primarily affect Agrin expression in vulnerable SMA motor neurons.

We next directly investigated Agrin expression at the NMJ of vulnerable and resistant muscles from WT and SMA mice by immunostaining (Figures 5C–5F). Focusing on innervated NMJs labeled by both synaptophysin and α-bungarotoxin, we found that Agrin is absent from one-half of the innervated NMJs in the vulnerable QL muscle from AAV9-GFP-injected SMA mice, but present in nearly all NMJs from WT mice (Figures 5C and 5E). Neither denervation nor loss of Agrin was observed at NMJs from the resistant tibialis anterior (TA) muscle of SMA mice (Figures 5D and 5F). Thus, SMN deficiency induces a selective loss of Agrin expression at NMJs that innervate vulnerable muscles in SMA mice. Importantly, Agrin expression at vulnerable SMA NMJs was restored by AAV9-Lsm10/11 in addition to AAV9-SMN (Figures 5C and 5E). In contrast, the decrease

Author Manuscript Author Manuscript Author Manuscript Author Manuscript

in pre-synaptic SV2B levels (Tejero et al., 2016) that we also found to be specific for NMJs in the QL, but not the TA, of SMA mice is only restored by AAV9-SMN (Figure S6), highlighting the specificity of Lsm10/11 co-expression in correcting the deficit of Agrin levels. Together, these results reveal that the disruption of Agrin expression at vulnerable NMJs is a specific downstream consequence of U7 snRNP dysfunction induced by SMN deficiency that contributes to neuromuscular pathology in SMA mice.

DISCUSSION

SMN is a multifunctional protein that is essential for NMJ biology as shown by muscle denervation being a hallmark of SMA pathology in both humans and mouse models (Mercuri et al., 2020; Tisdale and Pellizzoni, 2015; Wirth et al., 2020). Establishing causal links between the dysregulation of specific functions of SMN in RNA regulation and neuromuscular pathology is fundamental for understanding the molecular mechanisms of SMA. Through selective restoration of U7 snRNP biogenesis in SMA mice, our findings reveal a surprising role for SMN-mediated U7 snRNP assembly and histone mRNA 3′-end processing in controlling NMJ integrity through Agrin expression that is disrupted in motor neuron disease (Figure 6), uncovering an RNA-mediated pathogenic mechanism in SMA and linking U7 function to neuromuscular development.

We describe an effective strategy to enhance the cell's capacity for SMN-mediated assembly of U7 snRNP through overexpression of Lsm10 and Lsm11 proteins. The logic of our approach was that higher levels of these two U7-specific proteins would increase the cellular pool of SMN complexes primed for U7 snRNP assembly. Consistent with this hypothesis, early work pointed to the efficiency of snRNP core formation, rather than gene copy number or transcriptional regulation, as a potentially rate-limiting step in the biogenesis of U7, which is approximately 100-fold less abundant than spliceosomal snRNPs (Grimm et al., 1993; Stefanovic et al., 1995). This likely reflects the lower levels of Lsm10 and Lsm11 relative to Sm proteins and, in turn, the amount of specialized SMN complexes that mediate their assembly onto U7 snRNA (Pillai et al., 2001, 2003; Tisdale et al., 2013). Accordingly, we demonstrate that combined overexpression of Lsm10 and Lsm11 specifically enhances U7 snRNP assembly under normal conditions, as well as in SMN deficiency, albeit to a lesser extent. This enhancement does not occur by overexpressing Lsm10 or Lsm11 individually, highlighting the requirement of their co-expression for stimulation of U7 snRNP assembly. Importantly, Lsm10 and Lsm11 overexpression partially counteracts the decrease in U7 snRNP induced by SMN deficiency, leading to improved 3′-end processing of histone mRNAs in both cultured mammalian cells and tissues of SMA mice. Furthermore, the effects are highly selective because other RNA processing events affected by SMN deficiency but unrelated to U7 activity are not improved. The demonstration of selective functional enhancement of U7 snRNP assembly and histone mRNA processing established the necessary premise to evaluate the contribution of this SMN-dependent RNA pathway in SMA pathology.

Building on the approach described above, this study reveals a highly unanticipated requirement of U7 snRNP for the integrity of the neuromuscular system. Early post-natal increases in U7 snRNP assembly by AAV9-mediated co-expression of Lsm10 and Lsm11

Author Manuscript Author Manuscript Author Manuscript Author Manuscript

leads to significant improvement of several structural and functional defects of vulnerable NMJs in SMA mice. The effects include a robust correction of denervation and impaired synaptic transmission at NMJs, as well as decreased skeletal muscle atrophy, all of which are hallmarks of SMA pathology (Mercuri et al., 2020; Tisdale and Pellizzoni, 2015; Wirth et al., 2020). Owing to the inability of enhanced U7 snRNP assembly to prevent the death of SMA motor neurons, our approach can only capture the effects of Lsm10 and Lsm11 co-expression on impaired synaptic connectivity of surviving motor units, which is reflected by the lower degree of correction of NMJ denervation and neurotransmission relative to SMN restoration that also rescues motor neuron survival. Consistent with the lack of beneficial effects on the loss of proprioceptive synapses and survival of motor neurons, the behavioral outcome of Lsm10 and Lsm11 co-expression in SMA mice is also limited to modest improvement of motor function. A similar situation has previously been observed after specific correction of de-afferentation or the death of motor neurons in the same mouse model (Van Alstyne et al., 2018; Osman et al., 2020; Simon et al., 2017, 2019). Importantly, our results also establish the independent nature of the pathogenic cascades driving death and denervation of SMA motor neurons, which emerge as uncoupled SMN-dependent events triggered by distinct snRNP assembly defects and downstream dysregulation of RNA splicing (Van Alstyne et al., 2018; Simon et al., 2017, 2019) and histone mRNA 3′-end processing (this study), respectively. Together, these findings expand our knowledge of the relative requirement for specific functions of SMN in the sensory motor circuit and reinforce the conclusion that SMA pathology results from the compounded effects of multiple, independent cellular deficits driven by alterations of distinct RNA pathways regulated by SMN.

How could dysfunction of the U7 snRNP-histone mRNA processing axis affect highly specialized neuromuscular synapses located at the distal end of motor axons? Here, we show that SMN deficiency induces the selective loss of Agrin at NMJs of vulnerable muscles that undergo denervation, and that Agrin restoration by Lsm10/11 co-expression coincides with the correction of neuromuscular connectivity in SMA mice. While it is conceivable that other genes are affected by U7 snRNP dysfunction in SMA motor neurons, we specifically focused on Agrin owing to its established role in NMJ biology. Agrin is an essential synaptic organizing protein released by motor neurons that is required for the proper formation and maintenance of NMJs through its ability to cluster AChRs on the muscle surface (Burgess et al., 1999; Ferns et al., 1992; Gautam et al., 1996; Nitkin et al., 1987; Samuel et al., 2012). Our conclusion that Agrin directly mediates the beneficial effects of restoring U7 snRNP assembly on the neuromuscular phenotype of SMA mice is also supported by direct evidence that increasing Agrin expression or signaling improves NMJ pathology in SMA mice (Boido et al., 2018; Feng et al., 2021; Kaifer et al., 2020; Kim et al., 2017). Thus, irrespective of other potential U7-dependent gene changes, SMN regulates the expression of Agrin in motor neurons through U7 snRNP and disruption of this pathway contributes to neuromuscular dysfunction in SMA mice. These findings have potential translational implications; further mechanistic dissection of the SMN-dependent pathway highlighted here may provide therapeutic entry points to counteract NMJ deficits in SMA and other diseases. Recently, mutations in the *LSM11* and U7 (*RNU7*) genes have been linked to Aicardi-Goutières syndrome (AGS) (Naesens et al., 2022; Uggenti et al.,

Author Manuscript Author Manuscript Author Manuscript Author Manuscript

2020), and defective Agrin expression could contribute to some of the clinical features of AGS involving muscle dysfunction. The dysregulation of this pathway could also participate in the NMJ pathology of other neurodegenerative diseases like ALS, for which there is evidence of interference with SMN function (Sun et al., 2015; Yamazaki et al., 2012) and histone mRNA expression (Amlie-Wolf et al., 2015; Gadgil et al., 2021; Igaz et al., 2011), as well as mitigation of muscle denervation by enhanced Agrin signaling in mouse models (Cantor et al., 2018; Pérez-García and Burden, 2012).

Our findings reveal a highly surprising functional connection that links seemingly disparate biological processes such as SMN-mediated U7 snRNP assembly and 3′-end processing of histone mRNAs encoding the main protein constituents of chromatin with the neurobiology of synaptic connections between motor neurons and muscles (Figure 6). A multitude of regulatory mechanisms contribute to the establishment and refinement of synaptic connections of motor neurons with their target muscle during development as well as sustain these connections in adulthood (Burden et al., 2018; Sanes and Lichtman, 1999; Tintignac et al., 2015). Our findings identify the pathway of SMN-dependent, U7-mediated histone mRNA processing among these mechanisms, uncovering an unexpected facet of RNA regulation of motor neuron biology and disease. The only cellular function of both U7 snRNP and its core subunits Lsm10 and Lsm11 is in the 3′-end cleavage of histone mRNAs (Dominski and Marzluff, 2007; Marzluff et al., 2008; Pillai et al., 2001, 2003; Tisdale et al., 2013). Moreover, SMN deficiency disrupts histone mRNA processing in motor neurons (Tisdale et al., 2013) and acts cell autonomously within these disease-relevant cells to induce NMJ denervation in SMA mouse models (Fletcher et al., 2017; Gogliotti et al., 2012; Martinez et al., 2012; McGovern et al., 2015). Thus, the functional requirement of U7 snRNP biogenesis and histone mRNA 3′-end processing to maintain the integrity of NMJs through Agrin highlights a previously unappreciated demand for replication-dependent histone synthesis in motor neurons that broadens the relevance of this SMN-regulated RNA pathway beyond its canonical role in the process of genome replication in dividing cells. A plausible scenario is that the pathway of SMN-mediated U7 snRNP assembly ensures an adequate supply of histones for proper chromatin regulation and expression of essential genes for synaptic organization and function in motor neurons, which include but are not necessarily limited to Agrin. Beyond motor neurons, it is possible that enhanced U7 snRNP function may also contribute to improve neuromuscular pathology of SMA mice through non-cell autonomous mechanisms involving other cell types, including Schwann cells and skeletal muscle cells, which have been implicated in the disease process (Hunter et al., 2016; Kim et al., 2022; Kong et al., 2021).

Histone modifications and chromatin remodeling have multifaceted roles in the CNS (Borrelli et al., 2008; Maze et al., 2013), and interference with histone dynamics can induce cell-type-specific transcriptional changes in non-replicative cells and affect synaptic development and neuronal physiology (Korb et al., 2017; Maze et al., 2015; Nashun et al., 2015). Our discovery of a role for SMN in controlling the expression of a key factor for NMJ integrity through U7-dependent histone mRNA processing expands on the mechanisms by which histone metabolism contributes to synaptic formation and neuronal function as well as motor neuron disease.

Author Manuscript Author Manuscript Author Manuscript Author Manuscript

Limitations of the study

Our findings causally link disruption of SMN-mediated U7 snRNP assembly to loss of Agrin and NMJ pathology in SMA mice. However, the molecular mechanisms by which defects in the pathway of histone mRNA regulation would affect Agrin expression remain to be determined. Although our data may suggest an effect on transcription owing to impaired histone supply, the precise cascade of events has not been investigated and other mechanisms cannot be ruled out. In this context, it is in principle possible that Lsm10/Lsm11 proteins either alone or within the U7 snRNP may perform an unknown, non-canonical function that is unrelated to 3′-end processing of histone mRNAs and responsible for regulation of Agrin in motor neurons. This study leaves open also the question as to whether there are other genes beyond Agrin that are regulated by Lsm10/Lsm11 and/or U7 snRNP in motor neurons. Addressing these questions would require selective disruption of U7-mediated histone mRNA 3′-end processing in motor neurons of WT mice followed by multidisciplinary approaches to analyze the downstream consequences on chromatin structure and function as well as Agrin expression and NMJ biology. In addition to conclusively establishing the causal relationship of U7-dependent histone metabolism with Agrin expression, this phenocopy approach would also afford the opportunity to determine the entire spectrum of genes regulated by this pathway in motor neurons.

STAR★METHODS

RESOURCE AVAILABILITY

Lead contact—Further information and requests for resources and reagents should be directed to and will be fulfilled by the lead contact, Livio Pellizzoni (lp2284@cumc.columbia.edu).

Materials availability—All reagents generated in this study are available from the lead contact.

Data and code availability

- All data reported in this paper will be shared by the lead contact upon request.
- This paper does not report original code.
- Any additional information required to reanalyze the data reported in this paper is available from the lead contact upon request

EXPERIMENTAL MODEL AND SUBJECT DETAILS

Cell lines—HEK293T and NIH3T3 cells were cultured under 5%CO_2 at 37°C in Dulbecco's modified Eagle's medium with high glucose (Invitrogen) containing 10% of fetal bovine serum (HyClone), 2 mM glutamine (Gibco), and 10 μg/mL Gentamicin (Gibco). The NIH3T3-Smn_{RNAi} cell line used in this study was described previously (Lotti et al., 2012; Ruggiu et al., 2012). To generate stable NIH3T3 cell lines with overexpression of Lsm10 and/or Lsm11, NIH3T3-Smn_{RNAi} cells were transduced with the corresponding lentiviral vectors and selected with neomycin/G418 (0.5 mg/mL; for NIH3T3-Lsm10/Smn_{RNAi}), Hygromycin B (250 μg/mL; for NIH3T3-Lsm11/Smn_{RNAi}) or both antibiotics

Author Manuscript Author Manuscript Author Manuscript Author Manuscript

(for NIH3T3-Lsm10/Lsm11/Smn_{RNAi}). Depletion of endogenous Smn was induced by treatment with doxycycline (100 ng/mL) for 5 days prior to analysis. All cell lines tested negative for mycoplasma contamination.

Mouse models—All mouse studies were performed in accordance with the National Institutes of Health (NIH) Guidelines on the Care and Use of Animals, complied with all ethical regulations, and were approved by the Institutional Animal Care and Use Committee of Columbia University (Protocol Number AC-AABB1507). The SMND7 mouse line FVB.Cg-Grm7$^{Tg(SMN2)89Ahmb}$ Smn1^{tm1Msd} Tg(SMN2*delta7)4299Ahmb/J on a pure FVB/N genetic background was obtained from the Jackson Laboratory (Jax stock #005025) and used to generate SMA mice (*Smn*$^{-/-}$/*SMN2*$^{+/+}$/*SMNΔ7*$^{+/+}$). Mice were housed in a 12 h/12 h light/dark cycle with access to food and water *ad libitum*, and all efforts were made to minimize suffering. Mice from all experimental groups were inspected daily starting from birth and for the entire duration of the experiment by investigative staff with the required regulatory training for proper care and use of laboratory animals in research. For survival studies, humane endpoints were applied as per veterinary recommendation and the criteria used to determine when mice should be euthanized included severe dehydration, low body temperature, desertion by feeding mother, and loss of >20% of body weight from the previous day. Accordingly, weight, death, or any endpoints were monitored and recorded daily. Mice reaching any of these endpoints would be euthanized immediately by CO_2 inhalation followed by cervical dislocation. None of the mice reached the criteria for euthanasia. All experimental mice used for biochemical and morphological studies were analyzed at P11, except for mice used for laser capture microdissection which were sacrificed at P6. Mice of both sexes in equal proportions were used in all experiments and aggregated data are presented because gender-specific differences were not found. Genotyping was performed by PCR using tail DNA and primers listed in Table S1 as described previously (Fletcher et al., 2017).

METHOD DETAILS

DNA constructs—The open reading frames (ORFs) of mouse Lsm10 and Lsm11 were amplified from a cDNA library generated from NIH3T3 fibroblasts and cloned into pcDNA3 as fusions with a FLAG tag sequence at the amino terminus (Invitrogen). The resulting FLAG-tagged ORFs were then cloned into pRRL.PGK.IRES.Neo and pRRL.PGK.IRES.Hygro lentiviral vectors, which were generated by replacing the GFP sequence in the pRRL.SIN.cPPT.PGK-GFP.WPRE vector (Addgene plasmid #12252) with an IRES-Neomycin and IRES-Hygromycin cassette, respectively. To generate the CMV-driven Lsm10–2A-Lsm11 construct, DNA fragments corresponding to FLAG-Lsm10 and 2A-FLAG-Lsm11 were amplified by PCR using appropriate primers and cloned sequentially into pCDNA3. The 2A self-cleaving peptide sequence from the *Thosea asigna* virus has been previously described (Szymczak et al., 2004). The entire FLAG-Lsm10–2A-FLAG-Lsm11 cassette was excised from the resulting pCDNA3 plasmid and cloned downstream of the CMV enhancer and chicken β-actin hybrid (CAG) promoter in the dsAAV-CB plasmid harboring AAV2 inverted terminal repeats (ITRs) for the production of self-complementary AAV vectors (Foust et al., 2010). The constructs for the expression of GFP and human

Author Manuscript Author Manuscript Author Manuscript Author Manuscript

SMN from the same dsAAV-CB vector were previously described (Simon et al., 2019). All constructs were verified by DNA sequencing.

AAV9 production—AAV9 viral vectors packaged into serotype-9 capsid were custom produced by Vector BioLabs using triple-plasmid transfection of HEK293 T cells and purification by two rounds of CsCl gradient centrifugation. Vectors were concentrated using Amicon Ultracel centrifugal filter devices with a 30,000 nominal molecular weight limit (Millipore), titered by qPCR using the primers listed in Table S1, quality checked by SDS/PAGE and silver staining, and stored at −80°C until use.

Lentivirus production—Viral stocks pseudotyped with the vesicular stomatitis G protein (VSV-G) were prepared by transient co-transfection of HEK293 T cells (Open Biosystems) using the ViraPower™ Lentiviral Packaging Mix (Invitrogen) following manufacturer's instructions. Supernatant was collected 48 h post transfection and passed through a 0.45 μm syringe filter. Lentivirus was concentrated by ultracentrifugation using a Beckman SW28 swinging bucket rotor at 19,500 rpm for 2.5 h at 16°C, reconstituted in PBS, and stored at −80°C until use.

Animal procedures—All surgical procedures on postnatal mice were performed in accordance with the NIH guidelines and approved by the IACUC of Columbia University. ICV injections were performed in newborn mice anesthetized by isoflurane inhalation. A single injection was carried out using 5 μL of AAV9 virus containing ~1.0×10^{11} viral genomes in phosphate buffered saline (PBS) containing 5% glycerol, 0.001% Pluronic F-68, and 0.02% Fast Green dye (Sigma). After 30 min recovery, pups were placed in their breeder cage and monitored daily for survival, weight and righting time. Righting time was defined as the time for the pup to turn over on its limbs after being placed on its back. The cut-off test time for the righting reflex assay was 60 s to comply with IACUC guidelines. Mice were sacrificed and tissue collection was performed in a dissection chamber under continuous oxygenation (95%O_2/5%CO_2) in the presence of cold (~12°C) artificial cerebrospinal fluid (aCSF) containing 128.35 mM NaCl, 4 mM KCl, 0.58 mM NaH_2PO_4, 21 mM $NaHCO_3$, 30 mM D-Glucose, 1.5 mM $CaCl_2$, and 1 mM $MgSO_4$.

Electrophysiology—For recordings of the monosynaptic reflex, the intact *ex vivo* spinal cord preparation was transferred to a customized recording chamber after dissection and continuously perfused with aCSF at a temperature of 21°–25°C. The dorsal root and ventral root of the L1 segment were placed into suction electrodes for stimulation or recording, respectively. The extracellular recorded potentials were recorded in response to a brief (0.2 ms) orthodromic stimulation of the L1 dorsal root. The stimulus threshold was defined as the current at which the minimal evoked response was recorded in 3 out of 5 trials. Clampex (v10.2, Molecular Devices) software was used for data acquisition and Clampfit (v10.2, Molecular Devices) was used for data analysis. The monosynaptic component of the EPSP amplitude was measured from the onset of response to 3 ms. Measurements were taken from averaged traces of 5 trials elicited at 0.1 Hz. The function of NMJs of the QL muscle was assessed *ex vivo* as previously described (Fletcher et al., 2017). After the removal of the spinal cord, the remaining vertebral column with the ventral root L1-L3 in continuity to

Author Manuscript Author Manuscript Author Manuscript Author Manuscript

the QL was transferred to the recording chamber containing aCSF at a temperature of 21°–25°C. The ventral root L1 was placed into a suction electrode to stimulate the motor neuron axons. Visual twitching of the QL after stimulation of the ventral root L1 ensured proper stimulation of the muscle. Subsequently, to measure the compound muscle action potential (CMAP), a concentric bipolar electrode was inserted in the QL between the insertion point of ventral roots L1 and L2. The stimulus threshold was defined as the current at which the minimal evoked response was recorded in 3 out of 5 trials. The nerve was stimulated at 1, 2, 5 and 10X threshold to ensure a supramaximal stimulation of the muscle. The maximum CMAP amplitude (baseline-to-peak) was determined as the average from 5 measurements.

Laser capture microdissection—Isolation of motor neurons by laser capture microdissection was performed as previously described (Van Alstyne et al., 2018; Lotti et al., 2012). Briefly, Cholera toxin B (CTB) conjugated to Alexa 488 was delivered by intramuscular injection in the iliopsoas and QL muscles of wild type and SMA mice at P2 using a finely pulled glass microelectrode. The L1-L3 spinal segments were dissected from the injected mice at P6, embedded in OCT, and flash frozen prior to sectioning with a cryostat. Sections (14 μm) were mounted on PEN-membrane slides 2.0 (Zeiss), fixed in 100% ethanol for 15 s, and air dried for 30 s prior to microdissection of CTB^+ motor neuron somata using a DM6000B microscope equipped with a LMD6000 laser capture unit (Leica).

RNA analysis—Isolation of total RNA from mouse tissue and cultured cells was carried out using TRIzol reagent (Ambion) as per manufacturer's instructions followed by treatment with RNAse-free DNaseI (Ambion). cDNA was generated from 1 μg of total RNA using the RevertAid RT Reverse Transcription Kit (ThermoFisher) with a mixture of random hexamer and oligo dT primers. qPCR reactions were performed using 2.5% of the cDNA and Power SYBR Green PCR master mix (Applied Biosystem) in technical triplicates and normalized to endogenous Gapdh mRNA levels. Total RNA was purified from ~200 motor neurons per biological replicate using the Absolutely RNA Nanoprep Kit (Agilent). Amplified cDNA was prepared from total RNA using the Ovation PicoSL WTA System V2 Kit (NuGEN) and purified with the MinElute Reaction Cleanup Kit (Qiagen). RNA quality and quantity were assessed using a 2100 Bioanalyzer (Agilent). The primers used for RT-qPCR experiments are listed in Table S1. For Northern blot analysis, total RNA (2 μg) was analyzed by electrophoresis on a denaturing 8% polyacrylamide gel containing 8 M urea followed by transfer to a positively-charge Hybond nylon membrane (GE Healthcare). Radioactive antisense RNA probes were *in vitro* transcribed from DNA oligonucleotide templates in the presence of [α^{32}P]-UTP (3000 Ci/mmol; Perkin Elmer) using the MEGAshortscript T7 kit (Invitrogen) and purified by passing through a P-30 Tris Micro Bio-Spin Column (Bio-Rad). Prior to hybridization, labeled RNA probes were denatured at 70°C for 5 min and transferred to ice. Membranes were pre-hybridized for at least 30 min at 60°C in a rotary oven in ULTRAhyb-oligo hybridization buffer (Invitrogen). After pre-hybridization, labeled probe (1×10^6 cpm/mL of hybridization buffer) was added to the same hybridization buffer and incubated overnight at 60°C in a rotary oven. The membrane was washed two times for 30 min each in 2X SSC/0.5% SDS at 60°C and then exposed to either a phosphoscreen or X-ray film. Quantification was carried out using a Typhoon PhosphorImager (Molecular Dynamics). The sequences of probes used are listed in Table S1.

Author Manuscript Author Manuscript Author Manuscript Author Manuscript

Protein analysis—Total protein extracts were generated by cell lysis in SDS sample buffer (2% SDS, 10% glycerol, 5% β-mercaptoethanol, 60 mM Tris-HCl pH 6.8, and bromophenol blue), followed by brief sonication and boiling. Protein was quantified using the *RC DC*™ Protein Assay (Bio-Rad). For immunoprecipitation experiments, cell extracts were prepared by homogenization in ice cold RSB-100 buffer (100 mM NaCl, 10 mM Tris-HCl pH 7.4, 2.5 mM $MgCl_2$) containing 0.1% NP40, protease inhibitors (Pierce/Thermo Scientific), and phosphatase inhibitors (PhosSTOP; Roche/Sigma-Aldrich), followed by passing five times through a 27-gauge needle and centrifugation at 10,000 × g for 15 min at 4°C. Extract supernatant was quantified using the Bradford Quick Dye assay (Bio-Rad). Antibodies were bound to protein G-Sepharose (Sigma-Aldrich) in RSB-100 buffer containing 0.1% NP40, protease inhibitors, and phosphatase inhibitors for 2 h at 4°C. Following five washes with the same buffer, antibody-bound beads were incubated with 200 μg of cell extract for 2 h at 4°C with tumbling. Following five washes with the same buffer, samples were processed for either RNA or protein analysis. Bound RNAs were extracted by treatment with proteinase K (200 μg) diluted in proteinase K buffer (10 mM EDTA, 100 mM Tris-HCl pH 7.5, 300 mM NaCl, 2% SDS) for 20 min at room temperature with gentle agitation followed by phenol-chloroform extraction and ethanol precipitation. Immunoprecipitated RNA was analyzed by electrophoresis on a denaturing 8% polyacrylamide gel containing 8 M urea followed by Northern blotting. Proteins were eluted from beads by boiling in SDS sample buffer and analyzed by SDS/PAGE on 12% polyacrylamide gels followed by Western blotting as previously described (Ruggiu et al., 2012).

***In vitro* snRNP assembly—**Radioactive U1 and U7 snRNAs were generated by run-off transcription with T7 polymerase from linearized plasmid DNA templates in the presence of m^7G cap analog (Promega) using the MEGAshortscript T7 kit (Invitrogen) as previously described (Gabanella et al., 2005, 2007; Tisdale et al., 2013). Cell and tissue extracts were prepared in ice-cold reconstitution buffer (20 mM HEPES-KOH, pH 7.9, 50 mM KCl, 5 mM $MgCl_2$, 0.2 mM EDTA, 5% glycerol) containing 0.01% NP-40 and *in vitro* snRNP assembly reactions were carried out for 1 h at 30°C as previously described (Gabanella et al., 2005, 2007; Tisdale et al., 2013). Following treatment with heparin sulfate (5 mg/mL) and 2 M urea for 15 min at room temperature, reactions were immunoprecipitated with anti-SmB (18F6) antibodies for 2 h at 4°C in RSB-500 buffer (500 mM NaCl, 10 mM Tris-HCl, pH 7.4, 2.5 mM $MgCl_2$) containing 0.1% NP40, protease inhibitors (Pierce/Thermo Scientific), and phosphatase inhibitors (PhosSTOP; Roche/Sigma-Aldrich). Following antibody conjugation, beads were washed 5 times in RSB-500 buffer. Immunoprecipitated snRNAs were analyzed by electrophoresis on a denaturing 8% polyacrylamide gel containing 8 M urea followed by autoradiography. Quantification was done using a Typhoon PhosphorImager (Molecular Dynamics).

Immunohistochemistry and confocal microscopy—Freshly dissected spinal cords were immersion-fixed in 4% paraformaldehyde (PFA) in PBS overnight at 4°C. Specific lumbar segments were identified by the ventral roots, embedded in 5% agar and sectioned at 75 μm with a VT1000 S Vibratome (Leica). Sections were washed briefly in PBS and then blocked for 2 h at room temperature in 10% normal donkey serum (Millipore) in 0.01

Author Manuscript Author Manuscript Author Manuscript Author Manuscript

M PBS containing 0.4% Triton X-100, pH 7.4. Immunostaining, washing, and mounting were then performed as previously described (Van Alstyne et al., 2021). For NMJ analysis, freshly dissected QL and TA muscles were immersion-fixed in 4% PFA-PBS for 1 h at room temperature, followed by a PBS wash and cryoprotection in 30% sucrose overnight at 4°C. Muscle was then embedded in Optimal Cutting Temperature (OCT) compound (Fisher), frozen on dry ice, and sectioned at 30 μm with a CM3050 S cryostat (Leica) for processing by immunostaining as previously described (Van Alstyne et al., 2021). The antibodies used for these experiments are listed in Table S2. For myofiber analysis, freshly dissected triceps muscle was immersion-fixed in 4% PFA-PBS for 1 h at room temperature followed by a PBS wash. Muscle was then cryoprotected by incubation with a gradient of sucrose solutions from 10% sucrose to 30% sucrose in 0.1 M phosphate buffer, pH 7.4 for 1 h each time. Cryoprotected tissue was then removed from sucrose, embedded in OCT, and flash-frozen in liquid nitrogen-cooled 2-methyl butane (Sigma) prior to serial sectioning at 25 μm thickness onto Superfrost Plus glass slides (Fisher) using a CM3050 S cryostat (Leica). Slides were incubated in TBS containing 0.2% Triton-X for 30 min and then with a solution containing TRITC-conjugated phalloidin (Sigma-Aldrich) and DAPI (ThermoFisher Scientific) overnight at 4°C. The following day, slides were washed 3 times with TBS-T and mounted with a glass coverslip using Fluoromount-G (Southern Biotech) mounting media. All images were collected with an SP5 confocal microscope (Leica) running the LAS AF software (v2.5.2.6939) and analyzed off-line using the Leica LAS X software (v1.9.0.13747) from z-stack images. For motor neuron number quantification, images were acquired from all the 75 μm sections of L1 and L5 spinal segments using a 40X objective at 3 μm steps in the z-axis steps. Images for H2AX intensity analysis were acquired using a 40X objective at identical settings for WT and SMA samples at 3 μm steps and quantified by measuring the peak intensity per unit area of the nuclear region of motor neurons as previously described (Van Alstyne et al., 2018, 2021). For $VGluT1^+$ synapses quantification, images were acquired using a 40X objective throughout the entire thickness of 75μm L1 sections at 0.2 μm z-steps. The total number of $VGluT1^+$ synapses on soma was determined by counting all the corresponding inputs on the surface of each motor neuron cell body. Images for NMJ analysis were acquired using a 20X objective at 2 μm steps in the z-axis. Myofiber area was quantified using Fiji (v1.0) and manual identification of myofiber edges.

QUANTIFICATION AND STATISTICAL ANALYSIS

Results are expressed as mean and standard error of the mean (SEM) from at least three independent experiments and biological replicates unless otherwise indicated. The exact value and meaning of n for each data set can be found in the figure legends. Differences between two groups were analyzed by two-tailed unpaired Student's t-test and differences among three or more groups were analyzed by one-way ANOVA followed by the Tukey's *post hoc* tests for multiple comparisons as indicated. The Shapiro-Wilk test was performed to check for the normality of data distribution. Mann-Whitney or Kruskal–Wallis one-way analysis of variance by ranks were applied as indicated when the assumptions for parametric tests were not met. GraphPad Prism (v9.1.2) was used for all statistical analyses and p values are indicated as follows: *$p < 0.05$; **$p < 0.01$; ***$p < 0.001$; ****$p < 0.0001$.

Author Manuscript Author Manuscript Author Manuscript Author Manuscript

Supplementary Material

Refer to Web version on PubMed Central for supplementary material.

ACKNOWLEDGMENTS

We are grateful to Samie Jaffrey for comments and critical reading of the manuscript. We thank Brian Kaspar for providing the dsAAV-CB vector and Markus Ruegg for the kind gift of Agrin antibodies.

This work was supported by the Muscular Dystrophy Association (L.P.) and NIH grants NS079002 (S.T.), NS102451 (L.P.), NS114218 (L.P.), NS116400 (L.P.), NS078375 (G.Z.M.), and AA027079 (G.Z.M).

REFERENCES

Amlie-Wolf A, Ryvkin P, Tong R, Dragomir I, Suh E, Xu Y, Van Deerlin VM, Gregory BD, Kwong LK, Trojanowski JQ, et al. (2015). Transcriptomic changes due to cytoplasmic TDP-43 expression reveal dysregulation of histone transcripts and nuclear chromatin. PLoS One 10.

Boido M, de Amicis E, Valsecchi V, Trevisan M, Ala U, Ruegg MA, Hettwer S, and Vercelli A (2018). Increasing agrin function antagonizes muscle atrophy and motor impairment in spinal muscular atrophy. Front. Cell. Neurosci. 12, 17. [PubMed: 29440993]

Borrelli E, Nestler EJ, Allis CD, and Sassone-Corsi P (2008). Decoding the epigenetic language of neuronal plasticity. Neuron 60, 961–974. [PubMed: 19109904]

Burden SJ, Huijbers MG, and Remedio L (2018). Fundamental molecules and mechanisms for forming and maintaining neuromuscular synapses. Int. J. Mol. Sci. 19, E490. [PubMed: 29415504]

Burgess RW, Nguyen QT, Son YJ, Lichtman JW, and Sanes JR (1999). Alternatively spliced isoforms of nerve- and muscle-derived agrin: their roles at the neuromuscular junction. Neuron 23, 33–44. [PubMed: 10402191]

Cantor S, Zhang W, Delestrée N, Remédio L, Mentis GZ, and Burden SJ (2018). Preserving neuromuscular synapses in ALS by stimulating MuSK with a therapeutic agonist antibody. Elife 7, e34375. [PubMed: 29460776]

Carissimi C, Saieva L, Gabanella F, and Pellizzoni L (2006). Gemin8 is required for the architecture and function of the survival motor neuron complex. J. Biol. Chem. 281, 37009–37016. [PubMed: 17023415]

Dominski Z, and Marzluff WF (2007). Formation of the 3' end of histone mRNA: getting closer to the end. Gene 396, 373–390. [PubMed: 17531405]

Donlin-Asp PG, Bassell GJ, and Rossoll W (2016). A role for the survival of motor neuron protein in mRNP assembly and transport. Curr. Opin. Neurobiol. 39, 53–61. [PubMed: 27131421]

Eusebio A, Oliveri F, Barzaghi P, and Ruegg MA (2003). Expression of mouse agrin in normal, denervated and dystrophic muscle. Neuromuscul. Disord. 13, 408–415. [PubMed: 12798796]

Feng Z, Lam S, Tenn EMS, Ghosh AS, Cantor S, Zhang W, Yen PF, Chen KS, Burden S, Paushkin S, et al. (2021). Activation of muscle-specific kinase (Musk) reduces neuromuscular defects in the delta7 mouse model of spinal muscular atrophy (sma). Int. J. Mol. Sci. 22, 8015. [PubMed: 34360794]

Ferns M, Hoch W, Campanelli JT, Rupp F, Hall ZW, and Scheller RH (1992). RNA splicing regulates agrin-mediated acetylcholine receptor clustering activity on cultured myotubes. Neuron 8, 1079–1086. [PubMed: 1319184]

Fletcher EV, Simon CM, Pagiazitis JG, Chalif JI, Vukojicic A, Drobac E, Wang X, and Mentis GZ (2017). Reduced sensory synaptic excitation impairs motor neuron function via Kv2.1 in spinal muscular atrophy. Nat. Neurosci. 20, 905–916. [PubMed: 28504671]

Foust KD, Wang X, McGovern VL, Braun L, Bevan AK, Haidet AM, Le TT, Morales PR, Rich MM, Burghes AHM, and Kaspar BK (2010). Rescue of the spinal muscular atrophy phenotype in a mouse model by early postnatal delivery of SMN. Nat. Biotechnol. 28, 271–274. [PubMed: 20190738]

Author Manuscript Author Manuscript Author Manuscript Author Manuscript

Gabanella F, Carissimi C, Usiello A, and Pellizzoni L (2005). The activity of the spinal muscular atrophy protein is regulated during development and cellular differentiation. Hum. Mol. Genet. 14, 3629–3642. [PubMed: 16236758]

Gabanella F, Butchbach MER, Saieva L, Carissimi C, Burghes AHM, and Pellizzoni L (2007). Ribonucleoprotein assembly defects correlate with spinal muscular atrophy severity and preferentially affect a subset of spliceosomal snRNPs. PLoS One 2, e921. [PubMed: 17895963]

Gadgil A, Walczak A, Stępień A, Mechtersheimer J, Nishimura AL, Shaw CE, Ruepp MD, and Raczyńska KD (2021). ALS-linked FUS mutants affect the localization of U7 snRNP and replication-dependent histone gene expression in human cells. Sci. Rep. 11, 11868. [PubMed: 34088960]

Gautam M, Noakes PG, Moscoso L, Rupp F, Scheller RH, Merlie JP, and Sanes JR (1996). Defective neuromuscular synaptogenesis in agrindeficient mutant mice. Cell 85, 525–535. [PubMed: 8653788]

Gilhus NE, Tzartos S, Evoli A, Palace J, Burns TM, and Verschuuren JJGM (2019). Myasthenia gravis. Nat. Rev. Dis. Prim. 5, 30. [PubMed: 31048702]

Gogliotti RG, Quinlan KA, Barlow CB, Heier CR, Heckman CJ, and Didonato CJ (2012). Motor neuron rescue in spinal muscular atrophy mice demonstrates that sensory-motor defects are a consequence, not a cause, of motor neuron dysfunction. J. Neurosci. 32, 3818–3829. [PubMed: 22423102]

Grimm C, Stefanovic B, and Schuümperli D (1993). The low abundance of U7 snRNA is partly determined by its Sm binding site. EMBO J. 12, 1229–1238. [PubMed: 8458335]

Gromova A, and La Spada AR (2020). Harmony lost: cell–cell communication at the neuromuscular junction in motor neuron disease. Trends Neurosci. 43, 709–724. [PubMed: 32846148]

Hunter G, Powis RA, Jones RA, Groen EJN, Shorrock HK, Lane FM, Zheng Y, Sherman DL, Brophy PJ, and Gillingwater TH (2016). Restoration of SMN in Schwann cells reverses myelination defects and improves neuromuscular function in spinal muscular atrophy. Hum. Mol. Genet. 25, 2853–2861. [PubMed: 27170316]

Igaz LM, Kwong LK, Lee EB, Chen-Plotkin A, Swanson E, Unger T, Malunda J, Xu Y, Winton MJ, Trojanowski JQ, and Lee VMY (2011). Dysregulation of the ALS-associated gene TDP-43 leads to neuronal death and degeneration in mice. J. Clin. Invest. 121, 726–738. [PubMed: 21206091]

Kaifer KA, Villalón E, Smith CE, Simon ME, Marquez J, Hopkins AE, Morcos TI, and Lorson CL (2020). AAV9-DOK7 gene therapy reduces disease severity in Smn2B/- SMA model mice. Biochem. Biophys. Res. Commun. 530, 107–114. [PubMed: 32828271]

Kim J-H, Kang J-S, Yoo K, Jeong J, Park I, Park JH, Rhee J, Jeon S, Jo Y-W, Hann S-H, et al. (2022). Bap1/SMN axis in Dpp4+ skeletal muscle mesenchymal cells regulates the neuromuscular system. JCI Insight 7, e158380. [PubMed: 35603786]

Kim J-K, Caine C, Awano T, Herbst R, and Monani UR (2017). Motor neuronal repletion of the NMJ organizer, Agrin, modulates the severity of the spinal muscular atrophy disease phenotype in model mice. Hum. Mol. Genet. 26, 2377–2385. [PubMed: 28379354]

Kong L, Valdivia DO, Simon CM, Hassinan CW, Delestrée N, Ramos DM, Park JH, Pilato CM, Xu X, Crowder M, et al. (2021). Impaired prenatal motor axon development necessitates early therapeutic intervention in severe SMA. Sci. Transl. Med. 13, eabb6871. [PubMed: 33504650]

Korb E, Herre M, Zucker-Scharff I, Gresack J, Allis CD, and Darnell RB (2017). Excess translation of epigenetic regulators contributes to fragile X syndrome and is alleviated by Brd4 inhibition. Cell 170, 1209–1223.e20. [PubMed: 28823556]

Le TT, Pham LT, Butchbach MER, Zhang HL, Monani UR, Coovert DD, Gavrilina TO, Xing L, Bassell GJ, and Burghes AHM (2005). SMNDelta7, the major product of the centromeric survival motor neuron (SMN2) gene, extends survival in mice with spinal muscular atrophy and associates with full-length SMN. Hum. Mol. Genet. 14, 845–857. [PubMed: 15703193]

Lefebvre S, Buürglen L, Reboullet S, Clermont O, Burlet P, Viollet L, Benichou B, Cruaud C, Millasseau P, Zeviani M, et al. (1995). Identification and characterization of a spinal muscular atrophy- determining gene. Cell 80, 155–165. [PubMed: 7813012]

Author Manuscript Author Manuscript Author Manuscript Author Manuscript

Li DK, Tisdale S, Lotti F, and Pellizzoni L (2014). SMN control of RNP assembly: from post-transcriptional gene regulation to motor neuron disease. Semin. Cell Dev. Biol. 32, 22–29. [PubMed: 24769255]

Lotti F, Imlach WL, Saieva L, Beck ES, Hao LT, Li DK, Jiao W, Mentis GZ, Beattie CE, McCabe BD, and Pellizzoni L (2012). An SMN-dependent U12 splicing event essential for motor circuit function. Cell 151, 440–454. [PubMed: 23063131]

Martinez TL, Kong L, Wang X, Osborne MA, Crowder ME, Van Meerbeke JP, Xu X, Davis C, Wooley J, Goldhamer DJ, et al. (2012). Survival motor neuron protein in motor neurons determines synaptic integrity in spinal muscular atrophy. J. Neurosci. 32, 8703–8715. [PubMed: 22723710]

Marzluff WF, Wagner EJ, and Duronio RJ (2008). Metabolism and regulation of canonical histone mRNAs: life without a poly(A) tail. Nat. Rev. Genet. 9, 843–854. [PubMed: 18927579]

Maze I, Noh KM, and Allis CD (2013). Histone regulation in the CNS: basic principles of epigenetic plasticity. Neuropsychopharmacology 38, 3–22. [PubMed: 22828751]

Maze I, Wenderski W, Noh KM, Bagot RC, Tzavaras N, Purushothaman I, Elsässer SJ, Guo Y, Ionete C, Hurd YL, et al. (2015). Critical role of histone turnover in neuronal transcription and plasticity. Neuron 87, 77–94. [PubMed: 26139371]

McGovern VL, Iyer CC, Arnold WD, Gombash SE, Zaworski PG, Blatnik AJ 3rd, Foust KD, and Burghes AHM (2015). SMN expression is required in motor neurons to rescue electrophysiological deficits in the SMNDelta7 mouse model of SMA. Hum. Mol. Genet. 24, 5524–5541. [PubMed: 26206889]

Meister G, Buühler D, Pillai R, Lottspeich F, Fischer U, Buühler D, Pillai R, Lottspeich F, and Fischer U (2001). A multiprotein complex mediates the ATP-dependent assembly of spliceosomal U snRNPs. Nat. Cell Biol. 3, 945–949. [PubMed: 11715014]

Mercuri E, Pera MC, Scoto M, Finkel R, and Muntoni F (2020). Spinal muscular atrophy — insights and challenges in the treatment era. Nat. Rev. Neurol. 16, 706–715. [PubMed: 33057172]

Meunier FA, Schiavo G, and Molgó J (2002). Botulinum neurotoxins: from paralysis to recovery of functional neuromuscular transmission. J. Physiol. Paris 96, 105–113. [PubMed: 11755789]

Naesens L, Nemegeer J, Roelens F, Vallaeys L, Meuwissen M, Janssens K, Verloo P, Ogunjimi B, Hemelsoet D, Callens S, et al. (2022). Mutations in RNU7–1 weaken secondary RNA structure, induce MCP-1 and CXCL10 in CSF, and result in aicardi-goutières syndrome with severe end-organ involvement. J. Clin. Immunol, 1–13.

Nashun B, Hill PWS, Smallwood SA, Dharmalingam G, Amouroux R, Clark SJ, Sharma V, Ndjetehe E, Pelczar P, Festenstein RJ, et al. (2015). Continuous histone replacement by hira is essential for normal transcriptional regulation and de novo DNA methylation during mouse oogenesis. Mol. Cell 60, 611–625. [PubMed: 26549683]

Nitkin RM, Smith MA, Magill C, Fallon JR, Yao YM, Wallace BG, and McMahan UJ (1987). Identification of agrin, a synaptic organizing protein from Torpedo electric organ. J. Cell Biol. 105, 2471–2478. [PubMed: 2826489]

Nussbacher JK, Tabet R, Yeo GW, and Lagier-Tourenne C (2019). Disruption of RNA metabolism in neurological diseases and emerging therapeutic interventions. Neuron 102, 294–320. [PubMed: 30998900]

Osman EY, Van Alstyne M, Yen P-F, Lotti F, Feng Z, Ling KK, Ko C-P, Pellizzoni L, and Lorson CL (2020). Minor snRNA gene delivery improves the loss of proprioceptive synapses on SMA motor neurons. JCI Insight 5, 130574. [PubMed: 32516136]

Passini MA, Bu J, Roskelley EM, Richards AM, Sardi SP, O'Riordan CR, Klinger KW, Shihabuddin LS, and Cheng SH (2010). CNS-targeted gene therapy improves survival and motor function in a mouse model of spinal muscular atrophy. J. Clin. Invest. 120, 1253–1264. [PubMed: 20234094]

Pellizzoni L, Yong J, and Dreyfuss G (2002). Essential role for the SMN complex in the specificity of snRNP assembly. Science 298, 1775–1779. [PubMed: 12459587]

Pérez-García MJ, and Burden SJ (2012). Increasing MuSK activity delays denervation and improves motor function in ALS mice. Cell Rep. 2, 497–502. [PubMed: 22939980]

Pillai RS, Will CL, Lührmann R, Schümperli D, and Müller B (2001). Purified U7 snRNPs lack the Sm proteins D1 and D2 but contain Lsm10, a new 14 kDa Sm D1-like protein. EMBO J. 20, 5470–5479. [PubMed: 11574479]

Author Manuscript Author Manuscript Author Manuscript Author Manuscript

Pillai RS, Grimmler M, Meister G, Will CL, Lührmann R, Fischer U, and Schümperli D (2003). Unique Sm core structure of U7 snRNPs: assembly by a specialized SMN complex and the role of a new component, Lsm11, in histone RNA processing. Genes Dev. 17, 2321–2333. [PubMed: 12975319]

Ruggiu M, McGovern VL, Lotti F, Saieva L, Li DK, Kariya S, Monani UR, Burghes AHM, and Pellizzoni L (2012). A role for SMN exon 7 splicing in the selective vulnerability of motor neurons in spinal muscular atrophy. Mol. Cell Biol. 32, 126–138. [PubMed: 22037760]

Samuel MA, Valdez G, Tapia JC, Lichtman JW, and Sanes JR (2012). Agrin and synaptic laminin are required to maintain adult neuromuscular junctions. PLoS One 7, e46663. [PubMed: 23056392]

Sanes JR, and Lichtman JW (1999). Development of the vertebrate neuromuscular junction. Annu. Rev. Neurosci. 22, 389–442. [PubMed: 10202544]

Simon CM, Dai Y, Van Alstyne M, Koutsioumpa C, Pagiazitis JG, Chalif JI, Wang X, Rabinowitz JE, Henderson CE, Pellizzoni L, and Mentis GZ (2017). Converging mechanisms of p53 activation drive motor neuron degeneration in spinal muscular atrophy. Cell Rep. 21, 3767–3780. [PubMed: 29281826]

Simon CM, Van Alstyne M, Lotti F, Bianchetti E, Tisdale S, Watterson DM, Mentis GZ, and Pellizzoni L (2019). Stasimon contributes to the loss of sensory synapses and motor neuron death in a mouse model of spinal muscular atrophy. Cell Rep. 29, 3885–3901.e5. [PubMed: 31851921]

Stefanovic B, Hackl W, Luührmann R, and Schümperli D (1995). Assembly, nuclear import and function of U7 snRNPs studied by microinjection of synthetic U7 RNA into Xenopus oocytes. Nucleic Acids Res. 23, 3141–3151. [PubMed: 7667090]

Sun S, Ling SC, Qiu J, Albuquerque CP, Zhou Y, Tokunaga S, Li H, Qiu H, Bui A, Yeo GW, et al. (2015). ALS-causative mutations in FUS/TLS confer gain and loss of function by altered association with SMN and U1-snRNP. Nat. Commun. 6, 6171. [PubMed: 25625564]

Szymczak AL, Workman CJ, Wang Y, Vignali KM, Dilioglou S, Vanin EF, and Vignali DAA (2004). Correction of multi-gene deficiency in vivo using a single «self-cleaving» 2A peptide-based retroviral vector. Nat. Biotechnol. 22, 589–594. [PubMed: 15064769]

Tejero R, Lopez-Manzaneda M, Arumugam S, and Tabares L (2016). Synaptotagmin-2, and −1, linked to neurotransmission impairment and vulnerability in Spinal Muscular Atrophy. Hum. Mol. Genet. 25, 4703–4716. [PubMed: 28173138]

Tintignac LA, Brenner HR, and Rüegg MA (2015). Mechanisms regulating neuromuscular junction development and function and causes of muscle wasting. Physiol. Rev. 95, 809–852. [PubMed: 26109340]

Tisdale S, and Pellizzoni L (2015). Disease mechanisms and therapeutic approaches in spinal muscular atrophy. J. Neurosci. 35, 8691–8700. [PubMed: 26063904]

Tisdale S, Lotti F, Saieva L, Van Meerbeke JP, Crawford TO, Sumner CJ, Mentis GZ, and Pellizzoni L (2013). SMN is essential for the biogenesis of U7 small nuclear ribonucleoprotein and 3'-end formation of histone mRNAs. Cell Rep. 5, 1187–1195. [PubMed: 24332368]

Uggenti C, Lepelley A, Depp M, Badrock AP, Rodero MP, El-Daher MT, Rice GI, Dhir S, Wheeler AP, Dhir A, et al. (2020). cGAS-mediated induction of type I interferon due to inborn errors of histone pre-mRNA processing. Nat. Genet. 52, 1364–1372. [PubMed: 33230297]

Van Alstyne M, Simon CM, Sardi SP, Shihabuddin LS, Mentis GZ, and Pellizzoni L (2018). Dysregulation of Mdm2 and Mdm4 alternative splicing underlies motor neuron death in spinal muscular atrophy. Genes Dev. 32, 1045–1059. [PubMed: 30012555]

Van Alstyne M, Tattoli I, Delestrée N, Recinos Y, Workman E, Shihabuddin LS, Zhang C, Mentis GZ, and Pellizzoni L (2021). Gain of toxic function by long-term AAV9-mediated SMN overexpression in the sensorimotor circuit. Nat. Neurosci. 24, 930–940. [PubMed: 33795885]

Winkler C, Eggert C, Gradl D, Meister G, Giegerich M, Wedlich D, Laggerbauer B, and Fischer U (2005). Reduced U snRNP assembly causes motor axon degeneration in an animal model for spinal muscular atrophy. Genes Dev. 19, 2320–2330. [PubMed: 16204184]

Wirth B, Karakaya M, Kye MJ, and Mendoza-Ferreira N (2020). Twenty-five years of spinal muscular atrophy research: from phenotype to genotype to therapy, and what comes next. Annu. Rev. Genom. Hum. Genet. 21, 231–261.

Author Manuscript Author Manuscript Author Manuscript Author Manuscript

Yamazaki T, Chen S, Yu Y, Yan B, Haertlein TC, Carrasco MA, Tapia JC, Zhai B, Das R, Lalancette-Hebert M, et al. (2012). FUS-SMN protein interactions link the motor neuron diseases ALS and SMA. Cell Rep. 2, 799–806. [PubMed: 23022481]

Zhang Z, Pinto AM, Wan L, Wang W, Berg MG, Oliva I, Singh LN, Dengler C, Wei Z, and Dreyfuss G (2013). Dysregulation of synaptogenesis genes antecedes motor neuron pathology in spinal muscular atrophy. Proc. Natl. Acad. Sci. USA 110, 19348–19353. [PubMed: 24191055]

Author Manuscript Author Manuscript Author Manuscript Author Manuscript

Highlights

- Lsm10 and Lsm11 co-expression enhances U7 snRNP assembly
- Selective correction of histone gene dysregulation by Lsm10/11 in SMA models
- U7 snRNP dysfunction contributes to neuromuscular pathology in SMA mice
- SMN regulates Agrin expression at the NMJ through U7 snRNP

Author Manuscript Author Manuscript Author Manuscript Author Manuscript

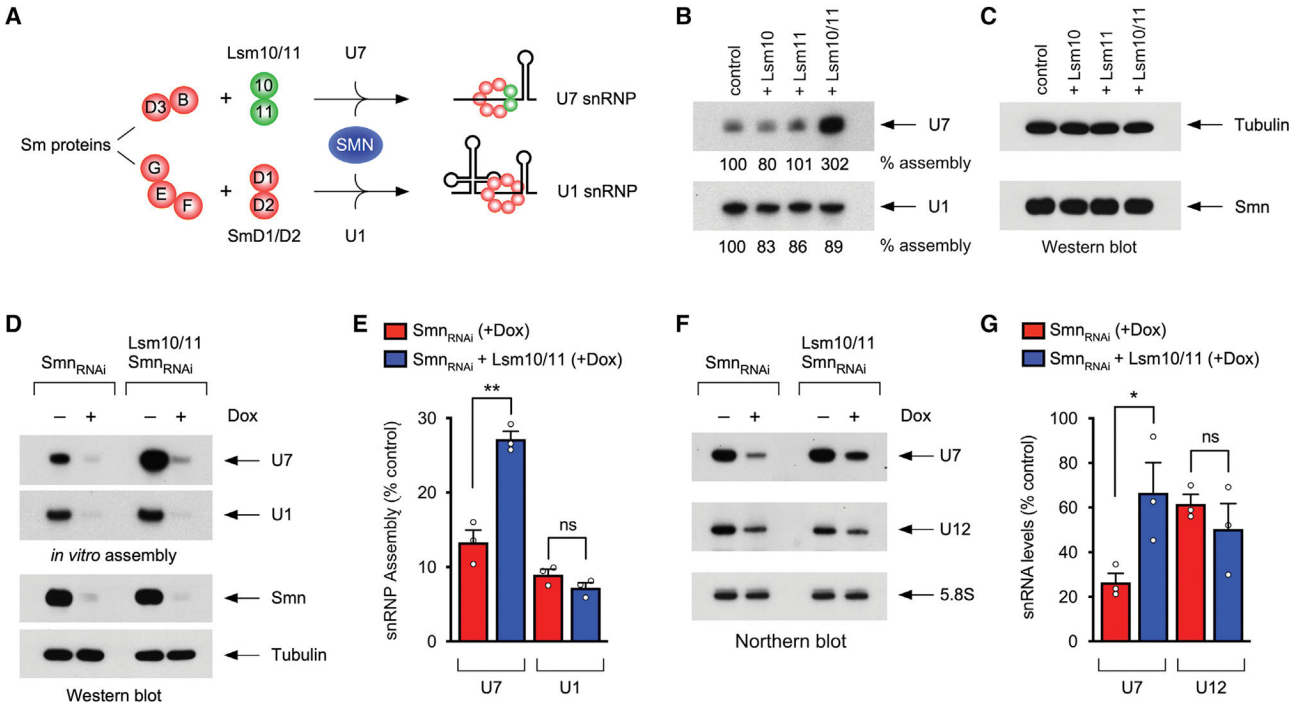

Figure 1. Co-expression of Lsm10 and Lsm11 promotes U7 snRNP assembly and prevents U7 snRNA reduction induced by SMN deficiency

(A) Schematic representation of SMN-mediated assembly of U7 and U1 snRNAs with their respective Sm and Lsm proteins.

(B) U7 and U1 *in vitro* snRNP assembly with extracts from NIH3T3-Smn_{RNAi} cell lines with or without overexpression of FLAG-tagged Lsm10 and Lsm11 as indicated. Quantification of snRNP assembly for each snRNA is shown as a percentage of control at the bottom of the corresponding panel.

(C) Western blot analysis of SMN levels in cell extracts used in (B).

(D) U7 and U1 *in vitro* snRNP assembly (top panels) and western blot analysis (bottom panels) with extracts from NIH3T3-Smn_{RNAi} and NIH3T3-Lsm10/11/Smn_{RNAi} cells treated with or without Dox for 5 days.

(E) Percentage of U7 and U1 snRNP assembly in Dox-treated cells relative to control NIH3T3-Smn_{RNAi} cells without Dox from experiments as in (D). Data are mean and standard error of the mean (n = 3 independent experiments). Statistics were performed with two-sided Student t-test. **$p < 0.01$; ns = not significant.

(F) Northern blot analysis of the indicated endogenous RNAs in the same experimental groups as in (D).

(G) Percentage of U7 and U1 snRNA levels in Dox-treated cells relative to control NIH3T3-Smn_{RNAi} cells without Dox from experiments as in (F). Data are mean and standard error of the mean (n = 3 independent experiments) normalized to 5.8 S rRNA. Statistics were performed with two-sided Student t test.

*$p < 0.05$; ns = not significant.

See also Figure S1.

Author Manuscript Author Manuscript Author Manuscript Author Manuscript

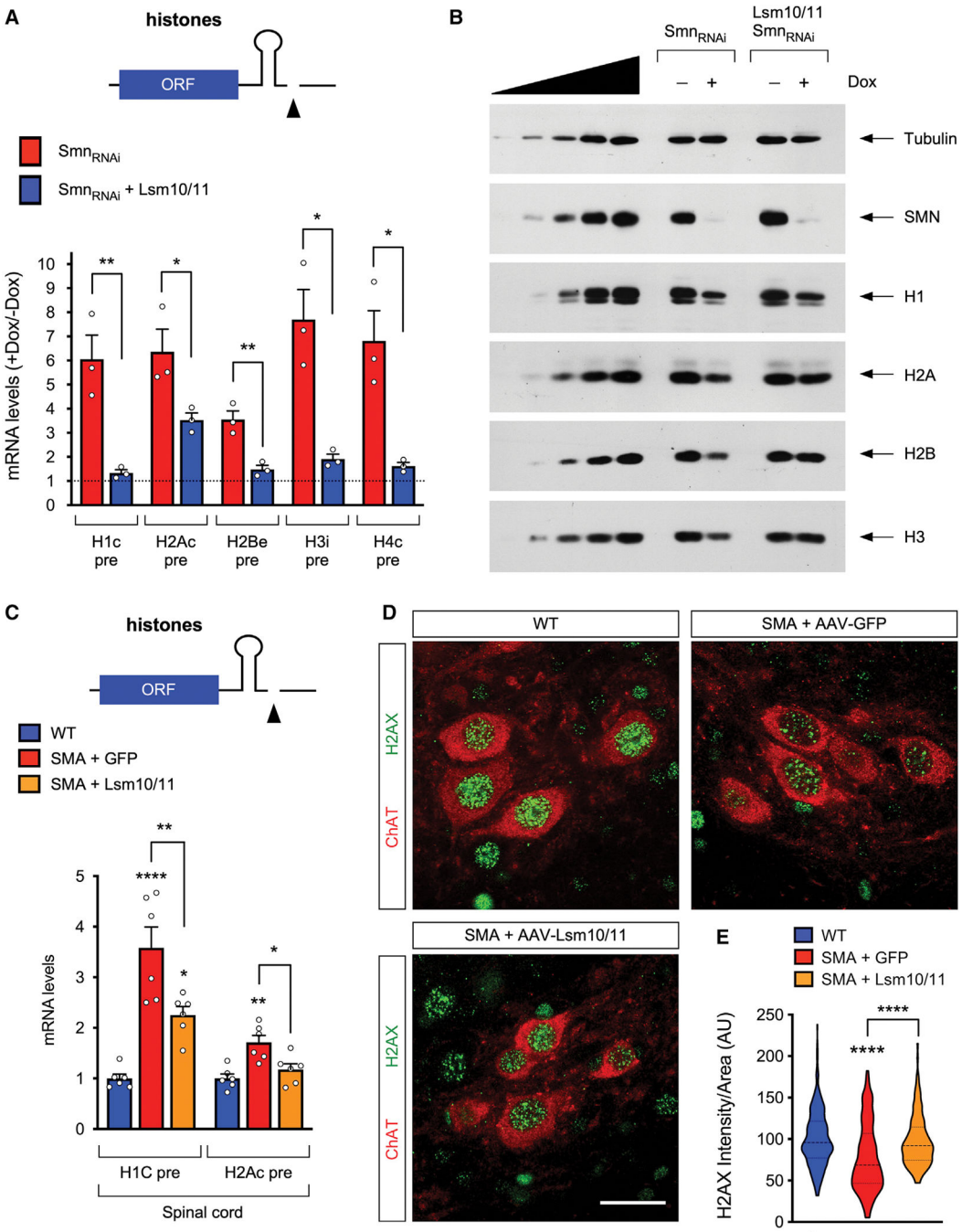

Figure 2. Co-expression of Lsm10 and Lsm11 corrects histone gene dysregulation induced by SMN deficiency

(A) RT-qPCR analysis of 3′-extended histone mRNA levels in NIH3T3-Smn$_{RNAi}$ and NIH3T3-Lsm10/11/Smn$_{RNAi}$ cells. Schematic representation of a histone pre-mRNA and the 3′-end cleavage is shown at the top. For each cell line, the fold change values in Dox-treated cells relative to untreated cells set as 1 are shown. Data are mean and standard error of the mean (n = 3 independent experiments) normalized to Gapdh mRNA. Statistics were performed with two-tailed Student t-test. *p < 0.05; **p < 0.01.

Author Manuscript Author Manuscript Author Manuscript Author Manuscript

(B) Western blot analysis of histone levels in NIH3T3-Smn_{RNAi} and NIH3T3-Lsm10/11/Smn_{RNAi} cells with or without Dox treatment. A two-fold serial dilution of control extract is shown on the left.

(C) RT-qPCR analysis of 3′-extended histone mRNAs in the spinal cord of SMA mice injected with AAV9-GFP or AAV9-Lsm10/11 relative to untreated WT mice at P11 set as 1. Schematic representation of a histone pre-mRNA and the 3′-end cleavage is shown at the top. Data are mean and standard error of the mean (n = 6 mice) normalized to Gapdh mRNA. Statistics were performed with one-way ANOVA with Tukey's post hoc test. *$p < 0.05$; **$p < 0.01$; ***$p < 0.001$.

(D) Histone H2AX and choline acetyltransferase (ChAT) immunostaining of L1 spinal cords from untreated WT mice and SMA mice injected with AAV9-GFP or AAV9-Lsm10/11 at P11. Scale bar, 20 μm. Note that images are pseudo-colored, and the green color does not represent the signal in the green fluorescence channel.

(E) Normalized fluorescent intensity of nuclear H2AX signal in $ChAT^+$ L1 motor neurons from experiments as in (D). The violin plots show the median (thick dotted line) and interquartile range (thin dotted lines) from the following number of motor neurons from three mice per group (n = 295 neurons for WT; n = 209 neurons for SMA + GFP; n = 178 neurons SMA + Lsm10/11). Statistics were performed with the Kruskal-Wallis test followed by Dunn's multiple comparisons test.

****$p < 0.0001$.

See also Figures S2, S3, and S4. ORF, open reading frame.

Author Manuscript Author Manuscript Author Manuscript Author Manuscript

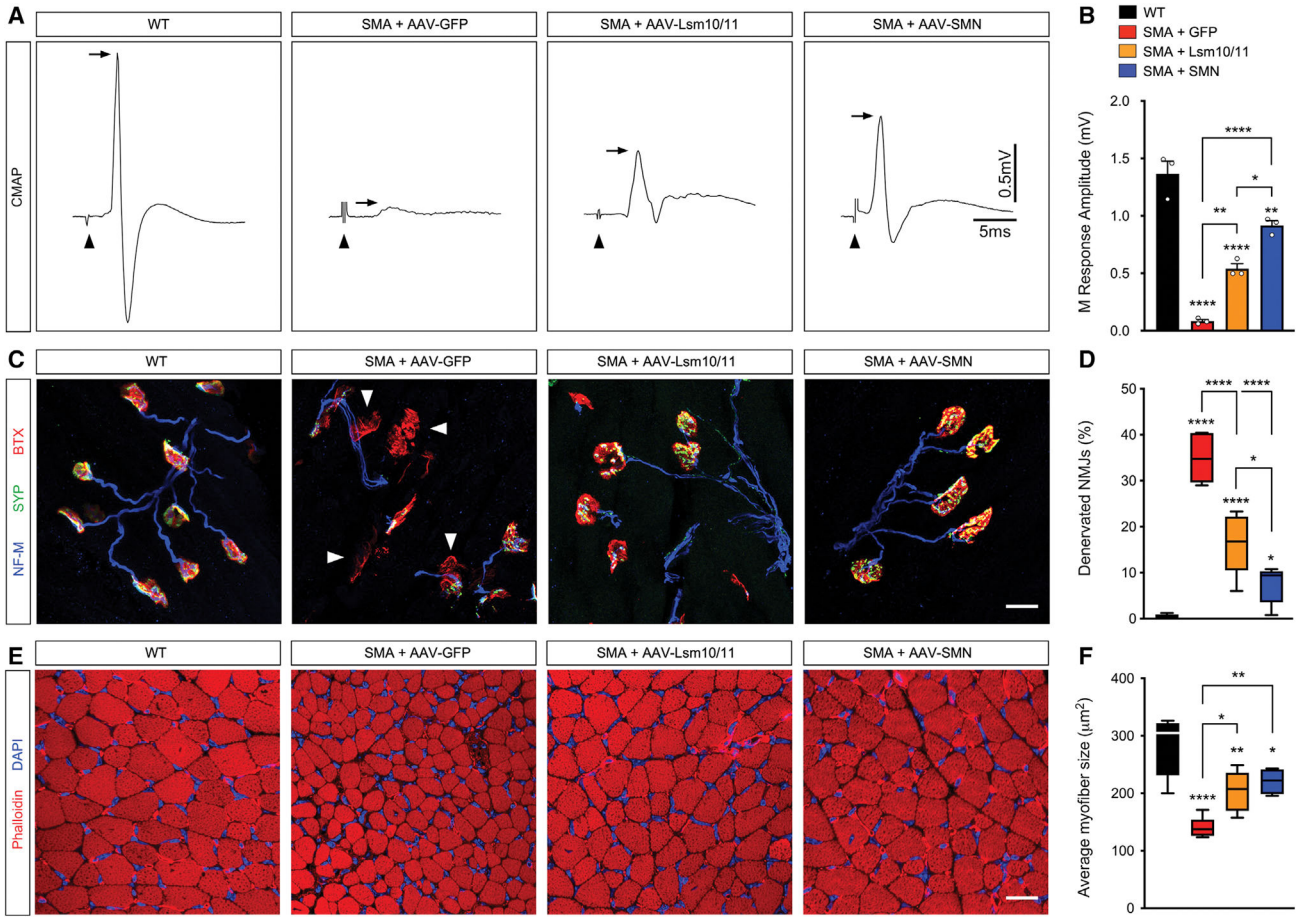

Figure 3. Co-expression of Lsm10 and Lsm11 corrects NMJ denervation and skeletal muscle atrophy in SMA mice

(A) Representative EMG tracings of compound muscle action potential (CMAP) recorded from the QL muscle of untreated WT mice and SMA mice injected with AAV9-GFP, AAV9-Lsm10/11 or AAV9-SMN at P11. Arrows indicate peak CMAP amplitude and arrowheads indicate artifact from stimulus.

(B) Amplitude of the M-response from the same groups as in (A) at P11. Data are mean and standard error of the mean (n = 3 mice). Statistics were performed with one-way ANOVA with Tukey's post hoc test. *p < 0.05; **p < 0.01; ****p < 0.0001.

(C) NMJ immunostaining with synaptophysin (SYP), neurofilament-M (NF-M) and α-bungarotoxin (BTX) of QL muscles from the same groups as in (A) at P11. Denervated NMJs lacking pre-synaptic SYP and NF-M staining are indicated by arrowheads. Scale bar, 20 μm.

(D) Percentage of fully denervated NMJs from experiments as in (C). The box-and-whiskers graph shows the median, interquartile range, and minimum and maximum from the following number of mice per group (n = 7 for WT, and SMA + GFP; n = 5 for SMA + Lsm10/11; n = 6 for SMA + SMN). Statistics were performed with one-way ANOVA with Tukey's post hoc test. *p < 0.05; ****p < 0.0001.

Author Manuscript Author Manuscript Author Manuscript Author Manuscript

(E) Tetramethylrhodamine B isothiocyanate (TRITC)-conjugated phalloidin and DAPI staining of cross sections of the triceps muscle from the same groups as in (A) at P11. Scale bar, 20 μm.

(F) Quantification of the average myofiber size (μm^2) from experiments as in (E). The box-and-whiskers graph shows the median, interquartile range, and minimum and maximum from the following number of mice (n = 5 for WT, SMA + Lsm10/11, and SMA + SMN; n = 6 for SMA + GFP). Statistics were performed with one-way ANOVA with Tukey's post hoc test. *$p < 0.05$; **$p < 0.01$; ****$p < 0.0001$.

See also Figure S5

Author Manuscript Author Manuscript Author Manuscript Author Manuscript

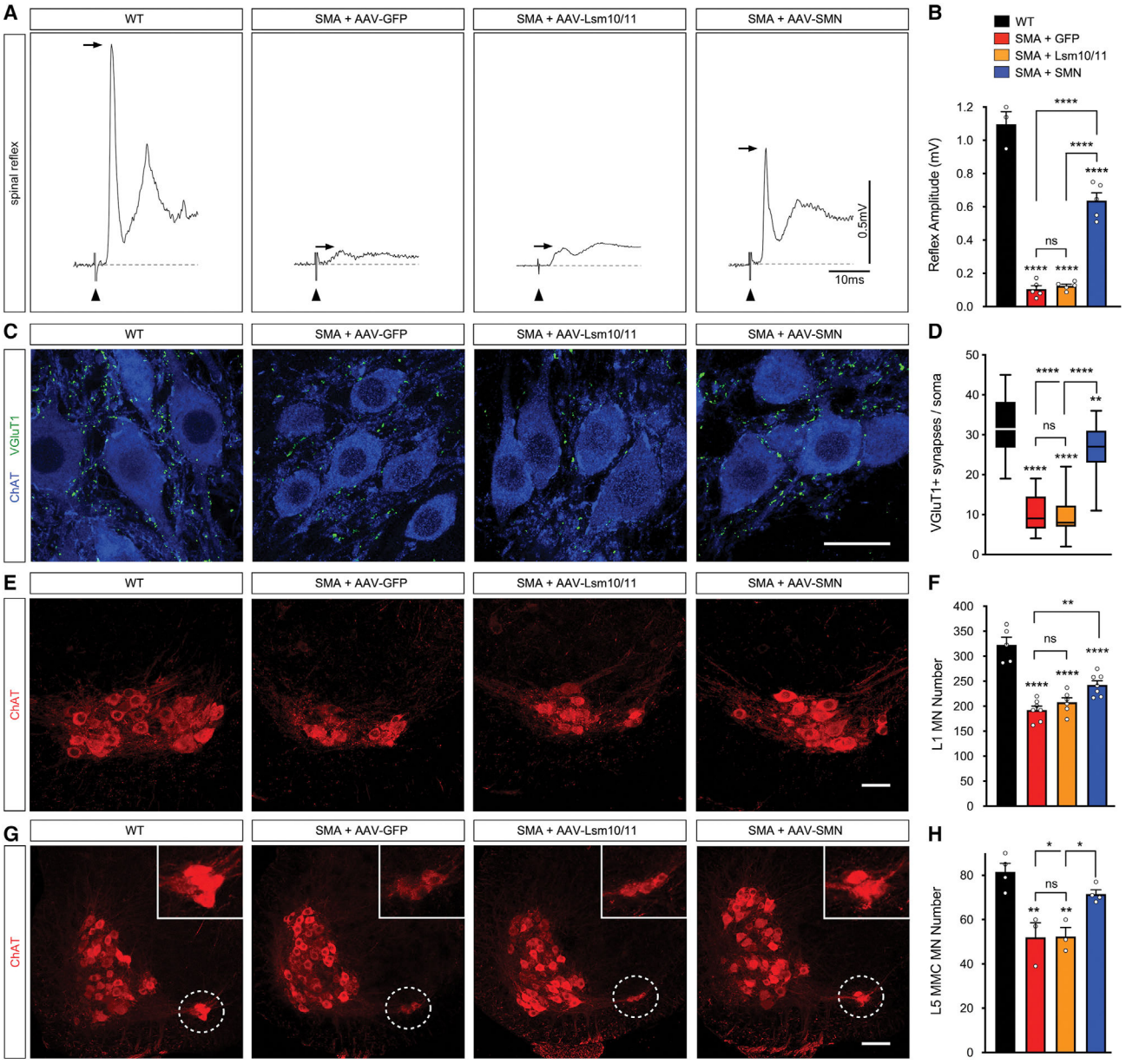

Figure 4. Co-expression of Lsm10 and Lsm11 does not correct spinal reflexes, the loss of proprioceptive synapses, or motor neuron death in SMA mice

(A) Representative traces of spinal reflexes recorded from the L1 ventral root after L1 dorsal root stimulation in uninjected WT mice and SMA mice injected with AAV9-GFP, AAV9-Lsm10/11, or AAV9-SMN at P11. Arrows indicate peak amplitude and arrowheads indicate the stimulus artifact.

(B) Spinal reflex amplitude from experiments as in (A). Data are mean and standard error of the mean (n = 3 mice for WT; n = 5 for each SMA injected group). Statistics were performed with one-way ANOVA with Tukey's post hoc test. ****p < 0.0001; ns = not significant.

(C) VGluT1 and choline acetyltransferase (ChAT) immunostaining of L1 spinal cords from the same groups as in (A). Scale bar, 20 μm.

Author Manuscript Author Manuscript Author Manuscript Author Manuscript

(D) Number of VGluT1$^+$ synapses on the somata of L1 motor neurons from experiments as in (C). The box-and-whiskers graph shows the median, interquartile range, and minimum and maximum from the following number of neurons and 3 mice per group (n = 22 neurons for WT; n = 25 neurons for SMA + GFP; n = 26 neurons for SMA + Lsm10/11; n = 21 neurons for SMA + SMN). Statistics were performed with one-way ANOVA with Tukey's post hoc test. **p < 0.01; ****p < 0.0001; ns = not significant.

(E) ChAT immunostaining of L1 spinal cords from the same groups as in (A). Scale bar, 50 μm.

(F) Total number of L1 motor neurons from experiments as in (E). Data are mean and standard error of the mean (n = 5 mice for WT; n = 7 mice for SMA + GFP and SMA + SMN; n = 6 mice for SMA + Lsm10/11). Statistics were performed with one-way ANOVA with Tukey's post hoc test. **p < 0.01; ****p < 0.0001; ns = not significant.

(G) ChAT immunostaining of L5 spinal cords from the same groups as in (A). L5 medial motor column (MMC) motor neurons are indicated by the dashed circle and shown magnified in the inset in (G). Scale bar, 125 μm.

(H) Total number of L5 MMC motor neurons from experiments as in (G). Data are mean and standard error of the mean (n = 4 mice for WT and SMA + SMN; n = 3 mice for SMA + GFP and SMA + Lsm10/11). Statistics were performed with one-way ANOVA with Tukey's post hoc test. *p < 0.05; **p < 0.01; ns = not significant.

Author Manuscript
Author Manuscript
Author Manuscript
Author Manuscript

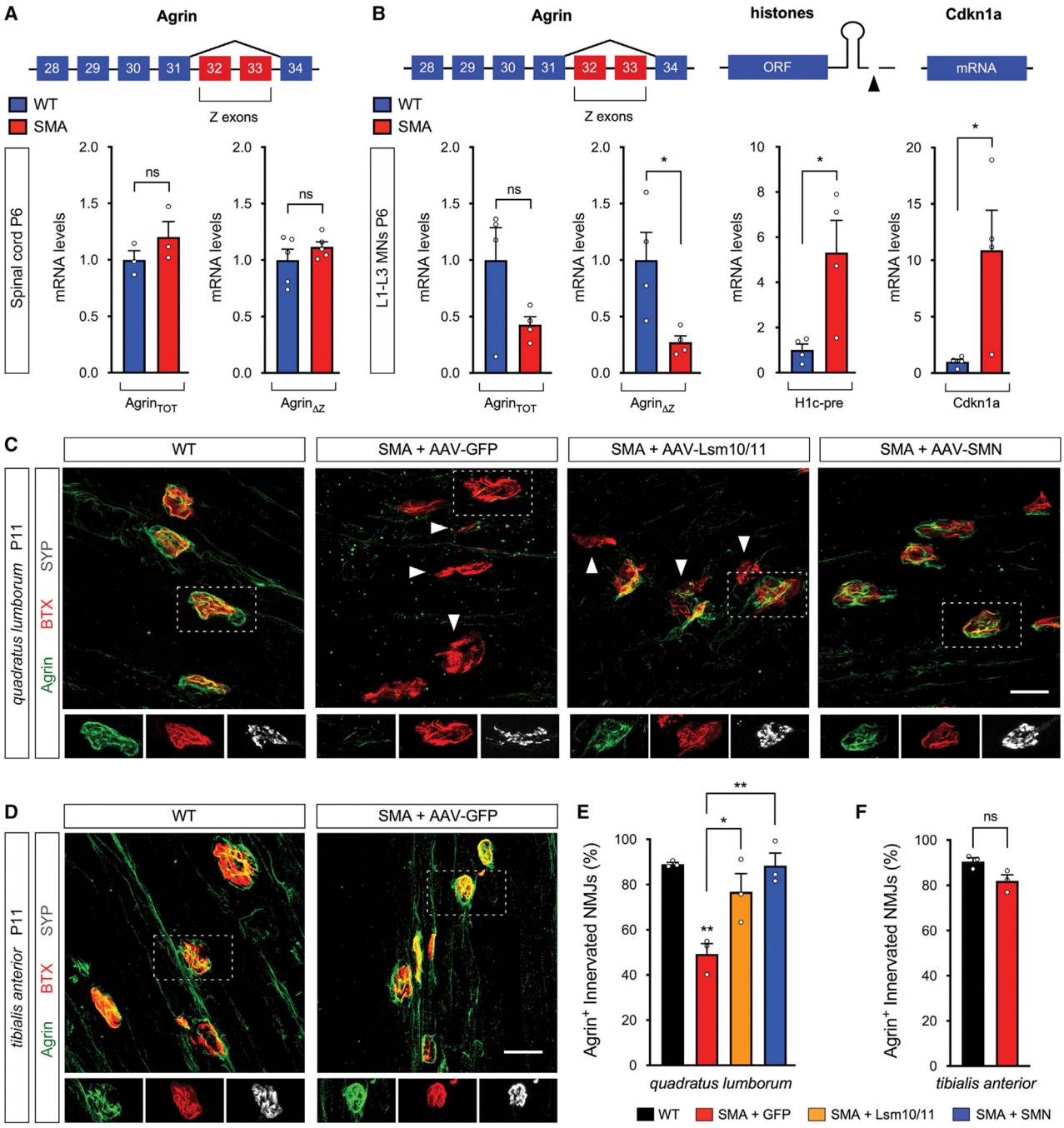

Figure 5. Lsm10/11 co-expression restores Agrin loss induced by SMN deficiency at vulnerable NMJs in SMA mice

(A) RT-qPCR analysis of total (TOT) and Z exon-skipped (ΔZ) Agrin mRNAs in the spinal cord of WT and SMA mice at P6. Schematic representation of Z exons and neighboring exons of Agrin mRNA is shown. Data are mean and standard error of the mean (n = 3 mice for $Agrin_{TOT}$; n = 5 mice for $Agrin_{\Delta Z}$) normalized to Gapdh and expressed relative to levels in WT mice set as 1. Statistics were performed with the two-tailed Student t-test. ns = not significant.

Author Manuscript Author Manuscript Author Manuscript Author Manuscript

(B) RT-qPCR analysis of $Agrin_{TOT}$ and $Agrin_{\Delta Z}$ mRNAs as well as 3′-extended histone H1c pre-mRNA and Cdkn1a mRNA in laser capture microdissected L1–L3 motor neurons from WT and SMA mice at P6. Data are mean and standard error of the mean (n = 4 independent experiments) normalized to Gapdh and expressed relative to levels in WT mice set as 1. Statistics were performed with the Mann-Whitney test. *$p < 0.05$; ns = not significant.
(C) NMJ immunostaining with Agrin, synaptophysin (SYP), and α-bungarotoxin (BTX) of QL muscles from untreated WT mice and SMA mice injected with AAV9-GFP, AAV9-Lsm10/11, or AAV9-SMN at P11. Denervated NMJs lacking pre-synaptic SYP staining are indicated by arrowheads and SYP staining is only shown for one representative innervated NMJ (dotted box) in the bottom insets. Scale bar, 20 μm.
(D) NMJ immunostaining with Agrin, SYP, and BTX of TA muscles from the same groups as in (C) at P11. SYP staining is only shown for one representative innervated NMJ (dotted box) in the bottom insets. Scale bar, 20 μm.
(E) Percentage of innervated NMJs that are $Agrin^+$ from experiments as in (C). Data are mean and standard error of the mean (n = 3 mice). Statistics were performed with one-way ANOVA with Tukey's post hoc test. *$p < 0.05$; **$p < 0.01$.
(F) Percentage of innervated NMJs that are $Agrin^+$ from experiments as in (D). Data are mean and standard error of the mean (n = 3 mice). Statistics were performed with two-sided Student t-test. ns = not significant; ORF = open reading frame.
See also Figure S6.

Author Manuscript Author Manuscript Author Manuscript Author Manuscript

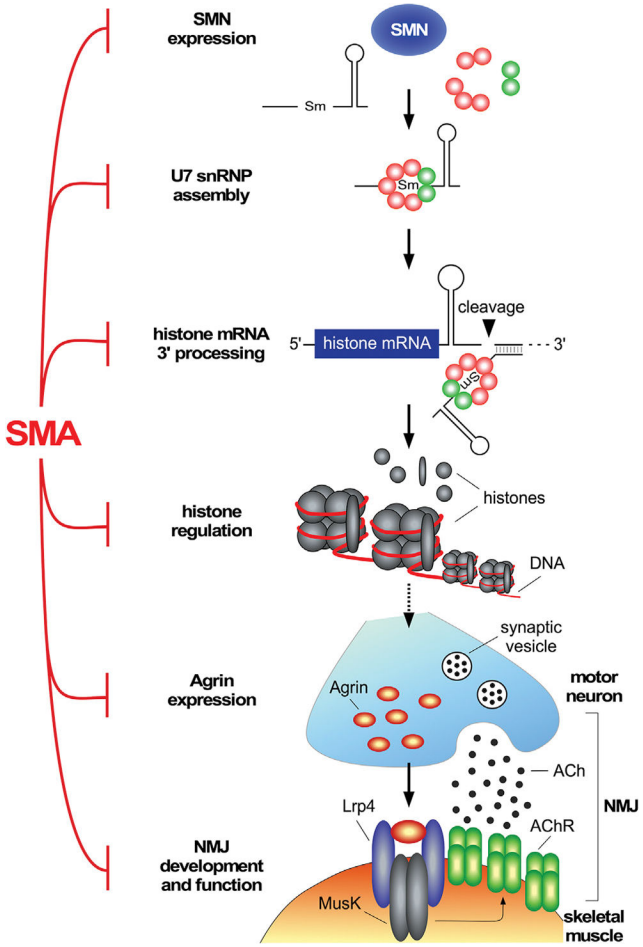

Figure 6. A model illustrating how U7 snRNP biogenesis dysfunction induced by SMN deficiency disrupts NMJ innervation in SMA

SMN controls normal assembly and biogenesis of U7 snRNP, which is required for proper 3′-end processing of histone mRNAs. In SMA, SMN deficiency disrupts U7 snRNP biogenesis leading to downstream dysregulation of histone gene expression including within post-mitotic motor neurons. Through mechanisms that remain to be established (dotted arrow), altered histone expression affects the normal expression of Agrin within motor neurons leading to decreased Agrin release at vulnerable NMJs, which in turn contributes to denervation and neuromuscular pathology in SMA mice.

Author Manuscript Author Manuscript Author Manuscript Author Manuscript

KEY RESOURCES TABLE

REAGENT or RESOURCE	SOURCE	IDENTIFIER
Antibodies		
Mouse monoclonal anti-SMN clone 8	BD Transd Lab	Cat#610646; RRID: AB_397973
Mouse monoclonal anti-Tubulin DM1A	Sigma	Cat#T9026; RRID: AB_477583
Chicken polyclonal anti-GFP	Aves	Cat#GFP-1020; RRID: AB_10000240
Guinea pig polyclonal anti-VGluT1	Fletcher et al., 2017	N/A
Guinea pig polyclonal anti-Synaptophysin	Synaptic Systems	Cat#101-004; RRID: AB_1210382
Rabbit polyclonal anti-Agrin	Eusebio et al., 2003	N/A
Rabbit polyclonal anti-Neurofilament	Millipore	Cat#AB1987; RRID: AB_91201
Goat polyclonal anti-ChAT	Millipore	Cat#AB144; RRID: AB_90650
Bungarotoxin	Invitrogen	Cat#T1175; RRID: AB_2313931
Rabbit polyclonal anti-Sv2b	Synaptic Systems	Cat#119-102; RRID: AB_887803
Mouse monoclonal anti-SmB (18F6)	Carissimi et al., 2006	N/A
Mouse monoclonal anti-FLAG clone M2	Sigma	Cat#F3165; RRID: AB_439685
Mouse immunoglobulin (IgG)	Sigma	Cat#I8765; RRID: AB_1163672
Mouse monoclonal anti-histone (pan)	Millipore* *formerly Chemicon	Cat#MAB052; RRID: AB_93968
Rabbit polyclonal anti-H2A	Millipore	Cat#07-146; RRID: AB_310394
Rabbit polyclonal anti-H2B	Abcam	Cat#ab1790; RRID: AB_302612
Rabbit polyclonal anti-H3	Abcam	Cat#ab1791; RRID: AB_302613
Rabbit monoclonal anti-H2A.X	Cell Signaling	Cat#7631; RRID: AB_10860771
Alexa-Fluor 488 donkey anti-rabbit	Jackson	711-545-152; RRID: AB_2313584
Alexa-Fluor 488 donkey anti-goat	Jackson	705-545-147; RRID: AB_2336933
Alexa-Fluor 488 donkey anti-chicken	Jackson	Cat#703-545-155; RRID: AB_2340375
Cy3 donkey anti-rabbit	Jackson	711-165-152; RRID: AB_2307443
Cy3 donkey anti-mouse	Jackson	715-165-150; RRID: AB_2340813
Cy3 donkey anti-goat	Jackson	705-165-147; RRID: AB_2307351
Cy5 donkey anti-goat	Jackson	705-175-147; RRID: AB_2340415
Cy5 donkey anti-guinea pig	Jackson	706-175-148; RRID: AB_2340462
HRP rabbit anti-chicken	Millipore	Cat#AP162P; RRID: AB_91653
HRP goat anti-mouse	Jackson	115-035-044; RRID: AB_2338503
HRP goat anti-rabbit	Jackson	111-035-003; RRID: AB_2313567
Bacterial and virus strains		
Lentivirus: pRRL.PGK.FLAG.mLsm10.IRES.Neo	This paper	N/A
Lentivirus: pRRL.PGK.FLAG.mLsm11.IRES.Hygro	This paper	N/A
Lentivirus: pRRL.PGK.FLAG.mLsm10-2A-FLAG.mLsm11.IRES.Hygro	This paper	N/A
AAV9: pscAAV9-CB-GFP	Simon et al., 2019	N/A
AAV9: pscAAV9-CB-SMN	Simon et al., 2019	N/A

Author Manuscript Author Manuscript Author Manuscript Author Manuscript

REAGENT or RESOURCE	SOURCE	IDENTIFIER
AAV9: pscAAV9-CB-FLAG-Lsm11-2A-FLAG-Lsm10	This paper	N/A
Chemicals, peptides, and recombinant proteins		
Phalloidin-Tetramethylrhodamine B isothiocyanate (TRITC)	Sigma-Aldrich	Cat#P1951
FastGreen FCF dye	Sigma-Aldrich	Cat#F7252
Doxycycline Hydrochloride	Fisher Scientific	Cat#BP26535
Hygromycin B	Thermo Fisher Scientific	Cat#10687010
G418 Sulfate/Geneticin	Thermo Fisher Scientific	Cat#10131035
10% PLURONIC F-68	Gibco	Cat#24040-032
[α^{32}P]-UTP (3000 Ci/mmol, 10 mCi/mL)	Perkin Elmer	Cat#BLU507H500UC
TRIzol Reagent	Invitrogen/Thermo Fisher Scientific	Cat#15596018
ULTRAhyb-oligo hybridization buffer	Invitrogen/Thermo Fisher Scientific	Cat#AM8663
Amersham Hybond-N+ nylon membrane	GE Healthcare	Cat#RPN303B
Optimal Cutting Temperature (O.C.T.) Compound	Scigen/Fisher Scientific	Cat#23-730-625
2-Methylbutane	Sigma-Aldrich	Cat#M32631
Fluoromount-G	SouthernBiotech	Cat#0100-01
Agar	Fisher Scientific	Cat#A360-500
Normal donkey serum	Millipore	Cat#S30-100ML
Critical commercial assays		
RevertAid RT Reverse Transcription Kit	Thermo Fisher Scientific	Cat#K1691
ViraPower™ Lentiviral Packaging Mix	Invitrogen	K497500
Power SYBR Green PCR Master Mix	Applied Biosystems/Thermo Fisher Scientific	Cat#4367659
MEGAshortscript T7 Transcription Kit	Invitrogen/Thermo Fisher Scientific	Cat#AM1354
CalPhos Mammalian Transfection Kit	Takara	Cat#631312
Ambion DNase I (RNase-free)	Invitrogen/Thermo Fisher Scientific	Cat#AM2222
Micro Bio-Spin Columns P-30 Tris RNase-Free	Bio-Rad	Cat#732-6250
Absolutely RNA Nanoprep Kit	Agilent	Cat#400753
Ovation Pico WTA System V2	NuGEN	Cat#3302
MinElute Reaction Cleanup Kit	Qiagen	Cat#28204
RC DC Protein Assay Kit	Bio-Rad	Cat#5000122
QuickStart Bradford 1X Dye Reagent	Bio-Rad	Cat#5000205
PhosSTOP phosphatase inhibitor tablets	Roche/Sigma-Aldrich	Cat#4906837001
Protease inhibitor tablets, EDTA-free	Pierce/Thermo Fisher Scientific	Cat#A32965
Protein G-Sepharose, Fast Flow	Sigma-Aldrich	Cat#P3296
Ribo m^7G Cap Analog	Promega	Cat#P1711
RNasin Ribonuclease Inhibitor	Promega	Cat#N2111
Amicon Ultracel centrifugal filter device, 30K Da	Fisher Scientific	Cat#UFC203024

Author Manuscript Author Manuscript Author Manuscript Author Manuscript

REAGENT or RESOURCE	SOURCE	IDENTIFIER
Experimental models: Cell lines		
Mouse: NIH3T3-Smn_{RNAi}	Lotti et al., 2012	N/A
Mouse: NIH3T3-Lsm10/Lsm11/Smn_{RNAi}	This paper	N/A
Human: HEK293 T	Thermo Scientific	Cat#HCL4517
Experimental models: Organisms/strains		
Mouse: FVB.Cg-Tg(SMN2*delta7)4299Ahmb Tg(SMN2)89Ahmb Smn1tm1Msd/J	The Jackson Laboratory	JAX:005025; RRID: ISMR_JAX:005025
Oligonucleotides		
RT-PCR oligonucleotides. Table S1	This paper	N/A
PCR oligonucleotides. Table S1	This paper	N/A
Northern blot probes. Table S1	This paper	N/A
Recombinant DNA		
pcDNA3	Invitrogen	N/A
pcDNA3-FLAG-Lsm10	This paper	N/A
pcDNA3-FLAG-Lsm11	This paper	N/A
pcDNA3-FLAG-Lsm10-2A-FLAG-Lsm11	This paper	N/A
pRRLSIN.cPPT.PGK-GFP.WPRE	Addgene	RRID: Addgene_12252
pRRL.PGK.FLAG-Lsm10.IRES.Neo	This paper	N/A
pRRL.PGK.FLAG-Lsm11.IRES.Hygro	This paper	N/A
pAAV-CB-FLAG-Lsm10-2A-FLAG-Lsm11	This paper	N/A
pAAV-CB-hSMN	Simon et al., 2019	N/A
pAAV-CB-GFP	Simon et al., 2019	N/A
pcDNA3-U1	Gabanella et al., 2007	N/A
pCR8-GW-U7	Tisdale et al., 2013	N/A
Software and algorithms		
Prism v9.1.2	GraphPad	N/A
LAS X v1.9.0.13747	Leica	N/A
LAS AF v2.5.2.6939	Leica	N/A
Clampex v10.2	Molecular Devices	N/A
Clampfit v10.2	Molecular Devices	N/A
ImageJ/Fiji v1.0	NIH	https://imagej.nih.gov/ij/